


Towards 30% Power Conversion Efficiency in Thin-Silicon Photonic-Crystal Solar Cells

Sayak Bhattacharya,^{1,*} Ibrahim Baydoun,¹ Mi Lin,^{1,2} and Sajeev John¹

¹*Department of Physics, University of Toronto, 60 St. George Street, Toronto, Ontario M5S 1A7, Canada*

²*College of Electronic Science and Technology, Shenzhen University, Shenzhen 518060, China*

 (Received 13 March 2018; revised manuscript received 4 September 2018; published 3 January 2019)

By direct numerical solution of Maxwell's equations and the semiconductor drift-diffusion equations, we demonstrate solar-power conversion efficiencies in the 29%–30% range in crystalline-silicon photonic-crystal solar cells. These 3–12- μm -thick photonic crystals, consisting of wavelength-scale inverted-pyramid arrays, absorb sunlight considerably in excess of the Lambertian limit due to wave-interference-based light trapping. It is suggested that the resulting optimized balance between bulk Auger recombination and solar absorption occurs for a silicon thickness of 10 μm , in contrast to previous estimates of more than 100 μm . Optimized n^+pp^+ doping profiles involving low p doping throughout most of the bulk and thin n^+ and p^+ doping at the emitter and base regions yield an ideal electronic response. For solar absorption restricted to the 300–1100-nm range, we obtain a short-circuit current of 42.5 mA/cm², an open-circuit voltage of nearly 0.8 V, and a fill factor of about 87%, provided that the surface recombination velocities are less than 100 cm/s. With inclusion of solar absorption in the 1100–1200-nm range through electronic-band-gap narrowing and the Urbach optical absorption edge, our wave-interference-based light trapping enables an additional photocurrent density of 1.09 mA/cm² for an overall power conversion efficiency of 30%. Under solar concentration by factors of 20 and 150, the power conversion efficiencies are increased to 32.5% and 33.5%, respectively.

DOI: [10.1103/PhysRevApplied.11.014005](https://doi.org/10.1103/PhysRevApplied.11.014005)

I. INTRODUCTION

Photovoltaics is vital to the ever-increasing global energy demand. As a competitive source of clean energy on a mass scale, a crucial requirement is low-cost, high-efficiency solar cells. The laws of thermodynamics set a maximum-possible solar-to-electrical-power conversion efficiency of a single-junction crystalline-silicon (*c*-Si) cell under 1-sun illumination at room temperature of 32.23% [1]. In practice, this efficiency is unattainable due to incomplete absorption of sunlight and unavoidable nonradiative recombination of photogenerated charge carriers. The indirect electronic band gap of silicon makes it a relatively weak absorber of sunlight in the 800–1100-nm range. Another important limitation in the case of silicon is non-radiative Auger recombination in the bulk of the solar cell. These two considerations lead to an optimum thickness of silicon based on the balance between adequate solar absorption and low bulk recombination loss. In previous work [2] this limit was determined with use of the concept of Lambertian light trapping [3]. In this picture, light is described by ray optics and is not endowed with any wave character. The Lambertian light-absorption limit

is defined through a series of assumptions, starting with a randomly rough top surface that exhibits no specular reflection to incoming sunlight and that randomly deflects incoming rays through a $\cos\theta$ probability distribution, where θ is the angle that the ray within the bulk silicon makes with respect to the surface normal. The deflected ray then bounces off a perfect back reflector and returns to the top surface. If the return angle is greater than the critical angle defined by $\sin\theta_c = 1/n$ (where n is the wavelength-dependent real part of the refractive index of silicon), then the light undergoes total internal reflection at the top surface. A simple argument [3] suggests that, on average, an incoming light ray will undergo n^2 bounces from the back reflector before escaping through the top surface. Consequently, the average path length of light in the solar cell is $4n^2$ times the actual cell thickness. While this argument is not rigorous, the resulting Lambertian absorption spectrum provides a valuable benchmark for gauging the efficacy of actual light-trapping architectures.

Through detailed consideration of recombination in well-passivated *c*-Si, Richter *et al.* [4] quantified Auger recombination as a function of dopant density and injection level at 300 K. Assuming perfect Lambertian light trapping and ignoring practical issues of front-contact shadowing and sheet resistance, this Auger model leads to a practical

*sayak.bhattacharya@utoronto.ca

efficiency limit of 29.43% for a single-junction, *c*-Si solar cell under 1-sun illumination [2]. This theoretical efficiency limit is attained at a thickness of 110 μm , where the optimum balance between Lambertian solar absorption and Auger recombination is realized in undoped *c*-Si. An important assumption behind this efficiency limit is that light trapping is limited by the ray optics, the Lambertian limit [3]. The optimum thickness of 110 μm is a result of the trade-off between increasing photocurrent density with increasing thickness and decreasing open-circuit voltage (V_{OC}) due to further bulk Auger recombination. Real-world solar cells, both present and past ones, typically absorb sunlight below the Lambertian limit. As a result, previous world-record efficiencies were attained with a silicon thickness considerably greater than 110 μm . The present world-record-holding heterojunction interdigitated back-contact *c*-Si cell uses a 165- μm -thick *n*-type bulk *c*-Si crystal with donor concentration $N_D = 1.5 \times 10^{15} \text{ cm}^{-3}$ [5]. This cell exhibits a conversion efficiency of 26.7%, an open-circuit voltage of 0.738 V, and a short-circuit current of 42.65 mA/cm² [6]. The loss analysis of the Kaneka cell shows that under ideal conditions, the maximum theoretical efficiency of the cell would be 29.1% in the case of perfect Lambertian light trapping [5]. Furthermore, because of unavoidable Auger recombination, the maximum V_{OC} attainable by any 165- μm -thick cell with $N_D = 1.5 \times 10^{15} \text{ cm}^{-3}$ is 0.761 V [2,5]. Therefore, it is impossible for any experimental 165- μm -thick cell, using the Lambertian light-trapping scheme, to surpass these theoretical upper bounds.

In this paper, we suggest a paradigm shift in achieving the highest possible power conversion efficiencies in silicon solar cells. This involves the fundamental concept that thin-film silicon can surpass the theoretical efficiency limits of thick-silicon solar cells. Unlike ray-tracing methods that suggest advantages with cell thickness beyond 100 μm , we consider the precise solution of Maxwell's equations that properly incorporates wave-interference corrections in the ray-optics picture. In the case of silicon photonic crystals (PhCs) with microstructure on the scale of the optical wavelength, this leads to a major change in the physical picture of light trapping and an optimum silicon thickness of close to 10 μm . Wave interference in thin-silicon photonic crystals enables solar absorption well above the Lambertian limit due to two fundamental effects. The first is the highly-non-Lambertian deflection of light rays entering the top surface. Instead of the $\cos\theta$ distribution, a large fraction of incident light is refracted in directions with group velocity nearly parallel to the interface. This is referred to as "parallel-to-interface refraction" (PIR) [7]. The second effect is the magnitude of the group velocity, which can be considerably less than the "effective-medium" speed of light. Wave interference gives rise to what are called "slow-light modes." These two effects are associated with the higher bands of the

electromagnetic spectrum in the photonic crystal and lead to a much longer dwell time in a thin film than anticipated by the Lambertian light-trapping arguments.

Reducing the bulk thickness would not only reduce both extrinsic and intrinsic recombination but would also cut the production cost of the required high-grade *c*-Si. Moreover, at 10- μm thickness, silicon is flexible and may have broader applications. At the same time, near-perfect photon absorption in the thinner *c*-Si cells is possible through wave-interference-based light trapping [8,9]. Harvesting of solar energy through coupling of sunlight into slow photonic modes of ultrathin *c*-Si PhCs was discussed previously with modulated nanowire [10,11] and slanted conical-pore [12] architectures. Arrays of slightly thicker inverted-pyramid [13–16] and parabolic-pore [17] photonic crystals have also been shown to support PIR and slow optical modes to increase the optical path length and dwell time of the photons, resulting in significantly increased absorption. Wave-interference-based strong resonances associated with PIR [7] are particularly significant to absorption enhancement in the 800–1100-nm wavelength range [17], where *c*-Si has weak intrinsic absorption. Photonic-crystal light trapping effectively offsets the detrimental aspects of the indirect electronic band gap of silicon, allowing it to absorb as much sunlight as direct-band-gap semiconductors. It also holds the key to surpassing the statistical ray-trapping (Lambertian) limit. This opens up a completely new possibility of single-junction solar cells with efficiencies exceeding the ray-optics-based theoretical limit of 29.43%.

Experimental studies [18] have demonstrated close-to-Lambertian-limit light trapping using a 35- μm -thick macroporous Si absorber. Attempts to theoretically [19] surpass the Lambertian limit have been made with rigorous coupled-wave analysis of photonic crystals. Mode-coupling theory has been used to suggest that conventional limits can be surpassed in nanophotonic structures [20]. External cavities have also been proposed [21] in this context. Through experimental measurements guided by rigorous numerical solution of Maxwell's equations, Kuang *et al.* [17] showed that the absorption of 300–1100-nm sunlight in a nonoptimized 10- μm -thick *c*-Si parabolic-pore PhC with a lattice constant of 1200 nm fabricated by reactive-ion etching results in a maximum achievable photocurrent density (MAPD) close to the Lambertian limit of 39.63 mA/cm². Considerably greater increase in the MAPD is expected by optimization of the parabolic-pore height-to-lattice-constant ratio. Numerical and experimental work using inverted-pyramid PhCs has shown close-to-Lambertian-limit light absorption in both 5- and 10- μm -thick *c*-Si [14]. Rigorous finite-difference time-domain (FDTD) study (using the Electromagnetic Template Library [22]) of a 1.6- μm -thick *c*-Si slanted conical-pore PhC showed [12] that it is possible to exceed the

Lambertian limit over the broad AM1.5G spectrum. Inverted-pyramid PhCs, on the other other hand, can be fabricated accurately on a mass scale by wet etching. The anisotropic etching property of KOH towards *c*-Si leads naturally to inverted pyramids with a side-wall angle of 54.7° , the angle between the (111) plane and the (100) plane of *c*-Si. Unlike the classic pyramid arrays with $10\text{-}\mu\text{m}$ base lengths [23] that can be described by ray optics, we consider the largely unexplored regime of micropyramid photonic crystals with wavelength-scale features and novel wave-optics phenomena. With use of a rigorous FDTD solution of Maxwell's equations, light trapping and absorption beyond the Lambertian limit were demonstrated [13] in an optimized $10\text{-}\mu\text{m}$ -thick *c*-Si inverted-micropyramid PhC. The optimum lattice constant in this case is 2500 nm , yielding a MAPD of 42.5 mA/cm^2 .

In a real-world *c*-Si cell, optical absorption throughout the wavelength range from 300 to 1200 nm is relevant to the generation of charge carriers. Recombination of these carriers is dominated by the Auger process and defect-induced trap states in the bulk and at surfaces. To isolate the various contributions to solar-cell efficiency and make a head-to-head comparison with previous literature, we discuss models in which solar absorption in the $1100\text{--}1200\text{-nm}$ range is either included or excluded. We also compare models in which the defect-induced carrier lifetimes are 1.2 or 10 ms . Finally, we isolate the role of the sheet resistance due to lateral carrier transport between widely separated electrical contact fingers. This leads to a sequence of slightly varying theoretical projections for the power conversion efficiencies with the different models. Nevertheless, an overarching conclusion from the various models is that an optimized $10\text{-}\mu\text{m}$ -thick *c*-Si photonic-crystal solar cell covering the entire available solar spectrum, with state-of-the-art carrier lifetime and sheet-resistance losses included, can provide a solar-to-electrical-power conversion efficiency of 30% .

In this article, we investigate thin ($3\text{--}12\text{-}\mu\text{m}$) *c*-Si solar cells that use double-layer antireflection coating (ARC) and wave-interference-based light trapping in carefully optimized inverted-pyramid PhCs that surpass the Lambertian limit. We use the MAPDs and absorption profiles obtained by solving Maxwell's equations as input to the carrier-generation and carrier-transport equations for the solar cells. A low doping level ($5 \times 10^{15}\text{ cm}^{-3}$) in the *p*-type bulk crystal ensures low bulk Auger recombination. The top and rear of the cell are diffused with highly doped donor-type and acceptor-type impurities, respectively, to form conformal n^+ and p^+ layers at the two ends of the cell. These provide a front surface field (FSF) and a back surface field (BSF) to deflect minority carriers from the surfaces and contacts. Our electronics design (described in Sec. II) is similar to the conventional passivated-emitter, rear-totally-diffused (PERT) architecture [24–28]. However, because of the reduced Auger recombination in our

thin-silicon cell, we predict a power conversion efficiency 5% (additive) higher than that of the best-available PERT cell. Using the optimized doping parameters for FSF and BSF regions (discussed in Sec. V and Appendix A), we calculate J - V characteristics of our proposed cells with different thicknesses. While thick cells, in general, absorb more sunlight for higher J_{SC} , the increased nonradiative bulk Auger recombination leads to lower V_{OC} , and lower conversion efficiency (η). We show that $10\text{ }\mu\text{m}$ is the optimum cell thickness for inverted-pyramid PhCs using wave-interference-based light trapping. Considering solar absorption in the $300\text{--}1100\text{-nm}$ wavelength range, our optimum $10\text{-}\mu\text{m}$ -thick cell with $N_A = 5 \times 10^{15}\text{ cm}^{-3}$ offers $\eta = 29.73\%$ at 25°C , with V_{OC} reaching 0.8 V . This surpasses the hypothetical upper bound of 29.57% based on Lambertian light trapping in a $110\text{-}\mu\text{m}$ -thick cell [2]. Under 20-sun illumination, our thin-silicon cell provides 32.5% efficiency. This efficiency saturates to 33.5% at 150-sun illumination. Including the effects of band-gap narrowing (BGN) [29] and phonon-assisted optical absorption in the Urbach optical absorption edge [30–33], we consider further solar absorption in the $1100\text{--}1200\text{-nm}$ range. Our wave-interference-based light trapping then provides an additional photocurrent density of 1.09 mA/cm^2 . Despite the slightly reduced V_{OC} of 0.79 V , the overall power conversion efficiency (at 1 sun) in our $10\text{-}\mu\text{m}$ -thick photonic crystal increases to 30.15% . This suggests a new paradigm for high-efficiency-solar-cell design beyond the current world record ($\eta = 26.7\%$) using, instead, a flexible $10\text{-}\mu\text{m}$ -thick sheet of *c*-Si.

II. SOLAR-CELL DESIGN AND NUMERICAL METHODS

Figure 1 shows the geometry of our thin-*c*-Si inverted-pyramid-PhC solar cell. The front surface of the *c*-Si bulk crystal is textured with a square lattice (photonic-crystal lattice constant a) of inverted pyramids. Each pyramid has a side-wall angle of $\alpha = 54.7^\circ$, determined by the anisotropic etching of KOH. The height, h , of each pyramid is given by $(a/2) \tan \alpha$. The overall thickness of the *c*-Si active layer is denoted by H . The front surface of the *c*-Si layer is covered with two conformal ARC layers of refractive indices n_i and thicknesses t_i , where $i = 1$ and $i = 2$ correspond to the top and bottom ARC layers, respectively. These two ARC layers also form the front passivation layer for the cell. The front-electrode fingers make contact with the *c*-Si layer through highly doped regions with donor impurities (n^+). The strong electric field between the highly doped, thin n^+ layer and *p*-type bulk keeps the minority carriers (holes) away from the front electrodes, while aiding in efficient collection of the photogenerated electrons. Similarly, the rear p^+ layer acts as the BSF region, aiding in efficient collection of holes. The Gaussian doping profiles of donor and

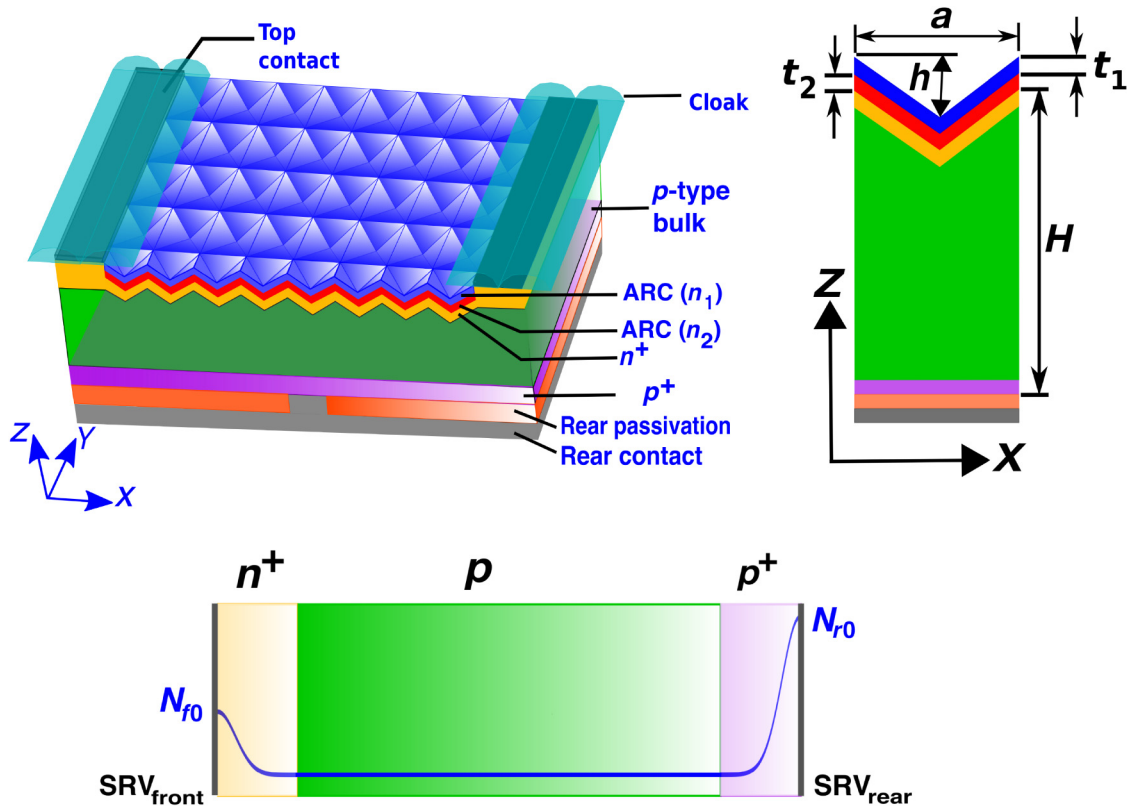


FIG. 1. Geometry of inverted-pyramid-PhC solar cell. Top left: Three-dimensional view of the cell showing different layers. n_1 and n_2 are the refractive indices of the double-layer ARC. Cloaking of the top contact could be a possible way to reduce shading loss [34–37]. Top right: Two-dimensional cross-section view of the unit cell of the PhC. The side-wall angle of the wet-etched pyramid is 54.7° (i.e., $h/(a/2) = \tan 54.7^\circ$). The thickness of the active layer is H . Bottom: Equivalent 1D model of the solar cell used in the semiconductor carrier-transport calculations. The blue line represents the schematic of the doping profile of the cell. N_{f0} and N_{r0} are the peak values of the Gaussian dopings of n^+ and p^+ regions, respectively.

acceptor impurities in the front n^+ and rear p^+ regions are characterized by $N_f = N_{f0} \exp(-z^2/2\sigma_f^2)$ and $N_r = N_{r0} \exp(-z^2/2\sigma_r^2)$, where N_{f0} and N_{r0} are the peak donor and acceptor doping concentrations (cm^{-3}) and σ_f and σ_r are the Gaussian widths (nm). For the n^+pp^+ cell, the acceptor doping concentration, N_A , throughout the p region is assumed to be $5 \times 10^{15} \text{ cm}^{-3}$ in all numerical computations.

The absorbed photon density in the solar cell is computed by finite-difference time-domain simulation [38], which produces excellent agreement with the experimentally measured absorption spectra of c -Si PhCs [17]. The Electromagnetic Template Library provides a stable FDTD scheme for solving Maxwell’s equations with accurate modeling of the frequency-dependent dielectric function of Si using modified Lorentz terms [39]. The top-right panel in Fig. 1 shows the cross section of the unit cell used for FDTD computations. The rear metal contact of the cell is modeled as a perfect electric conductor (PEC) and acts as a back reflector for sunlight. The rear passivation layer is implemented as a 50-nm SiO_2 ($n = 1.45$)

layer. This reduces parasitic absorption losses in real-world back contact such as silver [13] and justifies our modeling of the back reflector as a PEC. We apply periodic boundary conditions (PBCs) along the x and y directions and put perfectly matched layer at the computation boundaries normal to the z direction. The solar cell is illuminated with a normally incident broadband plane wave, coming from the $+z$ direction, that has significant energy in 300–1200-nm spectral range. For FDTD computations without BGN, we calculate the absorbed photon densities in the 300–1100-nm wavelength range and for those including BGN, we select the upper limit of the wavelength (λ_{max}) to be 1200 nm. This choice of λ_{max} includes two distinct effects. The first one is the electronic-band-gap narrowing of c -Si, denoted by ΔE_g (eV) and estimated with Schenk’s model [29] in our electronic calculations. The second effect, discussed in Sec. VI, includes a small amount of additional solar absorption available through the Urbach tail [30,31] below $(E_g - \Delta E_g)$ due to phonon-assisted absorption [32,33]. Here E_g is the unperturbed electronic band gap of Si. From FDTD computation, we

first calculate the absorption coefficient of *c*-Si as $A(\lambda) = 1 - R(\lambda) - T(\lambda)$, where $R(\lambda)$ and $T(\lambda)$ are the reflection and transmission coefficients of the structure. The MAPD of the cell under AM1.5G illumination is given by

$$J_{\text{MAPD}} = \int_{\lambda=300 \text{ nm}}^{\lambda_{\text{max}}} \frac{e\lambda}{hc} I(\lambda) A(\lambda) d\lambda, \quad (1)$$

where $I(\lambda)$ is the intensity of the AM1.5G spectrum and it is assumed that each absorbed photon creates a single electron-hole pair. For an ideal cell, without any surface and bulk recombination losses, the short-circuit current J_{SC} coincides with J_{MAPD} .

On the basis of the absorbed photon density and J_{MAPD} obtained from FDTD calculations, we model the electronic response of the three-dimensional (3D) solar cell by an equivalent one-dimensional (1D) model (shown in the bottom panel in Fig. 1). We also verify the accuracy of this 1D model by comparison with two-dimensional (2D) and 3D transport calculations. This microscopic 1D model enables optimization of the performance of the cell for different doping profiles, bulk recombination profiles, and surface recombination velocities (SRVs). Carrier-transport calculations are performed with SENTAURUS [40], with use of Shockley-Read-Hall (SRH) lifetimes (τ_{SRH}) of 1.2 and 10 ms as well as a state-of-the-art Auger recombination model [4]. An additive efficiency improvement of 0.5% is typically available if τ_{SRH} is increased to 10 ms. The simulation temperature is assumed to be 300 K, except when we compare the performance of our proposed cell with the performances determined at 25 °C [2]. Geometric details of the passivation layers and contacts in the 3D cell are subsumed into equivalent front and rear surface recombination velocities. These appear in the equivalent 1D transport as boundary conditions. In our 2D and 3D electronic transport models, distinct SRVs are chosen for contacts and insulating surface areas.

The overall solar-cell electronic response is dominated by the integrated solar absorption (MAPD) and is not strongly influenced by small variations in the spatial profile of absorption. Accordingly, we map the exact carrier-generation profile obtained by solving Maxwell's equations in the actual 3D photonic crystal to the 1D electronics model by a simple algorithm. For each optical wavelength we adopt a Beer-Lambert exponentially decaying absorption profile based on the complex, wavelength-dependent dielectric function of *c*-Si. The intensities of these exponentially decaying profiles are set according to the actual AM1.5G solar spectrum. An artificial carrier-generation profile is then obtained by integrating these profiles over the 300–1100-nm wavelength range. An artificial short-circuit current, J_{SC0} , is generated in the 1D model with use of SENTAURUS by initially ignoring Auger recombination, choosing τ_{SRH} to be very large, and setting the front and

rear SRVs to very-small values. This J_{SC0} (in the absence of losses) is smaller than J_{MAPD} from the 3D simulation of Maxwell's equations in the actual inverted-pyramid PhC. To compensate, we rescale the SENTAURUS 1D generation profile by a factor of $(J_{\text{MAPD}}/J_{\text{SC0}})$. This carrier-generation profile is used in the subsequent SENTAURUS computations that include realistic SRH, Auger, and surface recombination. We verify that this simplified algorithm reproduces with reasonable accuracy the current-voltage-characteristic curves obtained from a full-fledged solution of the 3D electronic transport equations using the exact carrier-generation profiles derived from Maxwell's equations.

To obtain good convergence for transport calculations with very thin n^+ and p^+ regions, an adaptive meshing strategy is used to ensure there are at least 20 mesh steps in the n^+ and p^+ regions. To resolve sharp changes in the highly doped regions with total widths less than 100 nm, at least 50 mesh steps are used. Adaptive meshes are denser in the regions where the doping profile changes rapidly, and vice versa. In Appendix B, we consider 2D carrier-transport calculations with the actual carrier-generation profile of the inverted-pyramid-PhC solar cell. Here the 3D carrier-generation profile, calculated by the FDTD method, is integrated along one of the lattice directions. The resulting 2D profile is repeated over a very large number of unit cells of the photonic crystal and mapped onto the SENTAURUS grid to simulate the effect of contact finger spacing much larger than the photonic-crystal lattice constant.

III. INVERTED MICROPYRAMIDS AND THEIR OPTIMIZATION

Pyramid and inverted-pyramid [23,41–45] surface structures have been useful in the design of classic solar cells that achieved previous world-record efficiencies. These conventional designs use architectures with length scales much larger than the wavelength of light to deflect sunlight in a classical ray-optics picture. In contrast, our inverted-micropyramid photonic crystals involve length scales and lattice constants comparable to the optical wavelength. In these “nonclassical” inverted pyramids, light propagation must be described with wave optics and the exact solution of Maxwell's equations. The resulting wave-interference-based light trapping is considerably more effective than with the classical counterparts.

The optimization study for our inverted-pyramid-PhC-based solar cell starts by identifying the optimum lattice constants for different cell thicknesses. Figure 2 shows the optimization results for $H = 3, 5, 7,$ and $10 \mu\text{m}$ in the absence of ARC layers. The corresponding optimum lattice constants are $a = 1300, 1800, 2100,$ and 2500 nm , respectively, with MAPDs of 36.31, 38.47, 38.79, and 39.57 mA/cm². With increasing cell thickness,

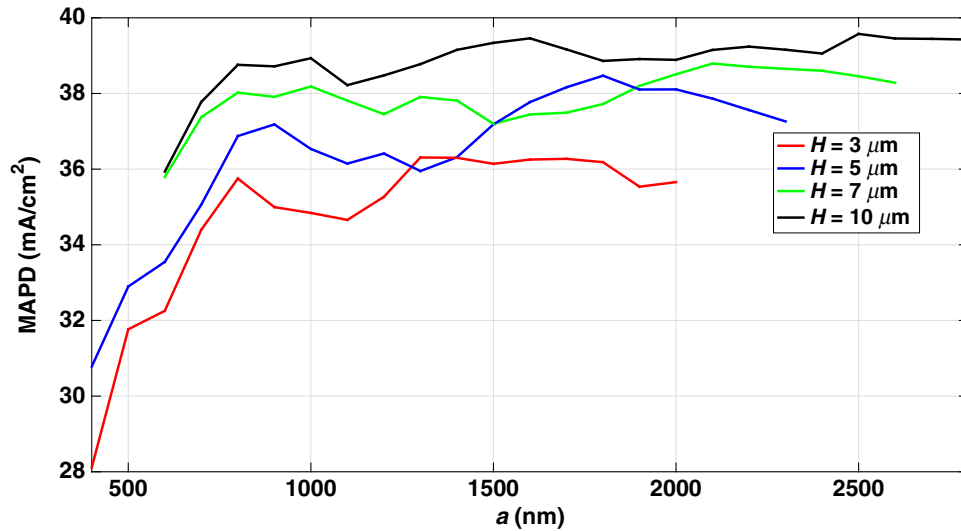


FIG. 2. Light-trapping optimization in 3–10- μm -thick inverted-pyramid photonic crystals (without an ARC layer). As the photonic crystal becomes thicker, the optimum lattice size shifts towards higher values.

the optimum value of the lattice constant shifts towards higher values. Next we optimize the refractive indices and thicknesses of the ARC layers. Table I summarizes the results of our optical optimization. Figure 3 compares the optimum MAPD variation against cell thickness for PhC solar cells with and without the optimum ARC layers (described in Table I). This shows that the double-layer ARC significantly increases the MAPD (by approximately 2.5–3 mA/cm^2) of the inverted-pyramid-PhC solar cells.

We associate some error margins with the MAPDs obtained from our time-domain numerical calculation that require careful consideration of narrow resonances to ensure accurate convergence. Sharp resonances lead to long-time temporal oscillations before complete absorption occurs. On the other hand, the MAPD in an actual experiment may be higher than we predict numerically. Fabrication-induced imperfections tend to smooth out very sharp resonances and the temporal oscillations in the long-wavelength range of the absorption spectra. This smoothing of the sharpest resonances can be simulated numerically by choosing a coarser

frequency resolution; in other words, a shorter simulation duration.

Figure 4 illustrates the change of the MAPD of the optimized, dual-ARC 10- μm -thick inverted-pyramid-PhC cell with respect to small variation Δa in the lattice constant around the optimum value of 2500 nm. For $0 < \Delta a < 200$ nm, the drop in the MAPD is no more than 0.22 mA/cm^2 , whereas for $-200 \text{ nm} < \Delta a < 0$, the MAPD drop is no more than 0.64 mA/cm^2 . For $a < 2400$ nm, the MAPD drops more slowly. As seen in Fig. 2, the 10- μm -thick structure without ARC exhibits a very high MAPD for lattice constants as small as 800 nm. The MAPDs at $a = 1000$ and 1600 nm are only slightly below the absolute maximum value at $a = 2500$ nm. Clearly, our optimized PhC structure exhibits high tolerance to moderate lattice variations and disorder.

Other possible sources of the decrease in the MAPD in a real-world cell are off-normal incidence of light and encapsulation with glass or ethylene vinyl acetate (EVA). Numerical results presented in [12] showed that PhC solar cells, in general, exhibit excellent angular response up to an off-normal angle of incidence of 50° without substantial

TABLE I. Summary of optical optimization in the 300–1100-nm wavelength range for inverted-pyramid PhC solar cells without BGN.

H (μm)	a (nm)	n_1	n_2	t_1 (nm)	t_2 (nm)	MAPD corresponding to the Lambertian limit (mA/cm^2)	MAPD in inverted-pyramid-PhC solar cell (mA/cm^2)
3	1300	1.4	2.6	95	45	36.64	39.05 ± 0.1
5	1800	1.4	2.7	90	40	38.03	40.93 ± 0.1
7	2100	1.4	2.5	100	45	38.85	41.81 ± 0.1
10	2500	1.4	2.6	100	45	39.63	42.50 ± 0.1
12	2700	1.4	2.6	100	45	40.01	42.75 ± 0.1
15	3100	1.4	2.6	100	45	40.44	43.03 ± 0.1

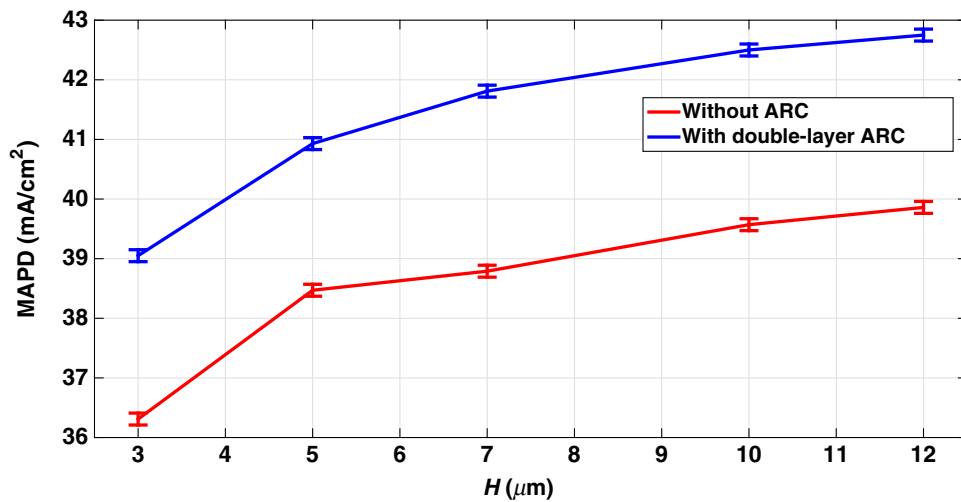


FIG. 3. Variation of MAPD in the 300–1100-nm wavelength range with cell thickness. Optimization of the refractive indices and widths of the double-layer conformal ARC increases the MAPD by 2.5–3 mA/cm². The error bars correspond to ± 0.1 mA/cm² uncertainty in the computed MAPDs.

degradation of the MAPD. The PIR modes of the PhC are excited with light incident within a 50° cone around the normal [7]. Standard EVA or glass encapsulation reduces the MAPD of the PhC. However, it was shown in Ref. [46] that for lattice constants larger than 1000 nm, an additional 130-nm-thick layer of planar ARC, with a refractive index of 1.27, on the top of EVA or glass enables similar or better antireflection performance as compared with the original air-ARC-PhC system.

The carrier-generation rates within the *c*-Si region of various inverted-pyramid-PhC solar cells are shown in Fig. 5. The 3D carrier-generation rate within the PhC unit cell is integrated along one lattice direction (*y* direction in this case). The triangular regions at the top of the generation profiles have a side-wall angle of approximately 54.7° . Figures 5(a)–5(c) show the carrier-generation rates for optimized 3-, 5- and 7- μm -thick cells, respectively. Although the optimum lattice constants are different for cells with $H = 3, 5,$ and $7 \mu\text{m}$, the carrier-generation profiles exhibit very similar distributions. For the optimum

10- μm -thick cell with $a = 2500$ nm, the peak carrier-generation rate [shown in Fig. 5(d)] is smaller by more than 1 order of magnitude in comparison with the thinner cells but the peak-generation region near the top of the cell is more extended.

Figure 6 shows the absorption spectra of the optimized inverted-pyramid-PhC solar cells with thicknesses ranging from 3 to 10 μm . The inset shows the sub-band absorption (over the 1100–1200-nm wavelength range) in the 10- μm -thick inverted-pyramid-PhC cell. The sub-band absorption is discussed in detail in Sec. VI.

In this paper we consider the optimization with respect to only the inverted-pyramid lattice constant and antireflection coating. Additional optimization can be performed through the shaping of the lower contact protrusions that touch the p^+ doping layer through gaps in the bottom SiO₂ passivation layer. For example, it has been shown [47] that with an ultrathin active-layer thickness of $H = 1.6 \mu\text{m}$, plasmonic resonances in the lower contact can lead to a MAPD of 38 mA/cm².

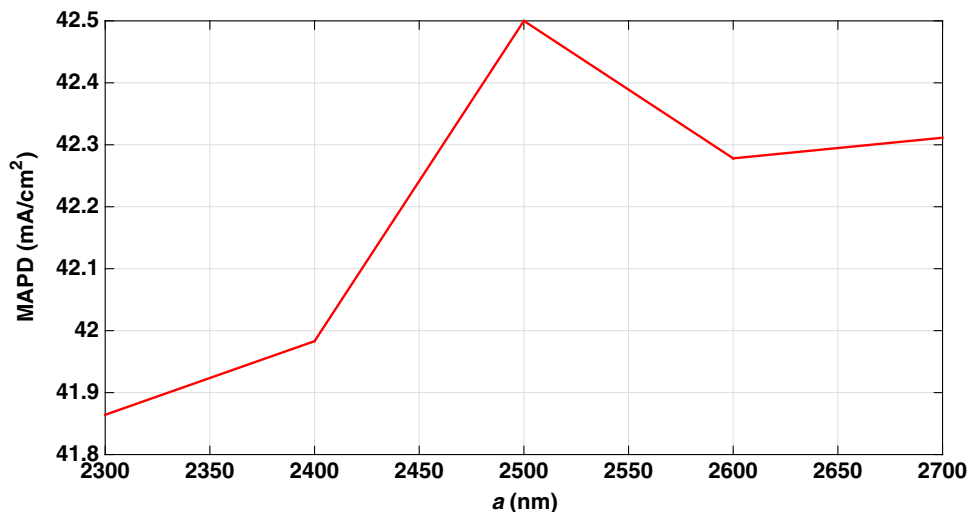


FIG. 4. MAPD variation of the anti-reflection (AR)-coated 10- μm -thick cell with lattice constant. The parameters for the dual-layer ARC are $n_1 = 1.4$, $n_2 = 2.6$, $t_1 = 100$ nm, and $t_2 = 45$ nm. For a ± 200 -nm variation of the lattice constant around the optimum value of 2500 nm, the MAPD reduction is less than 0.64 mA/cm².

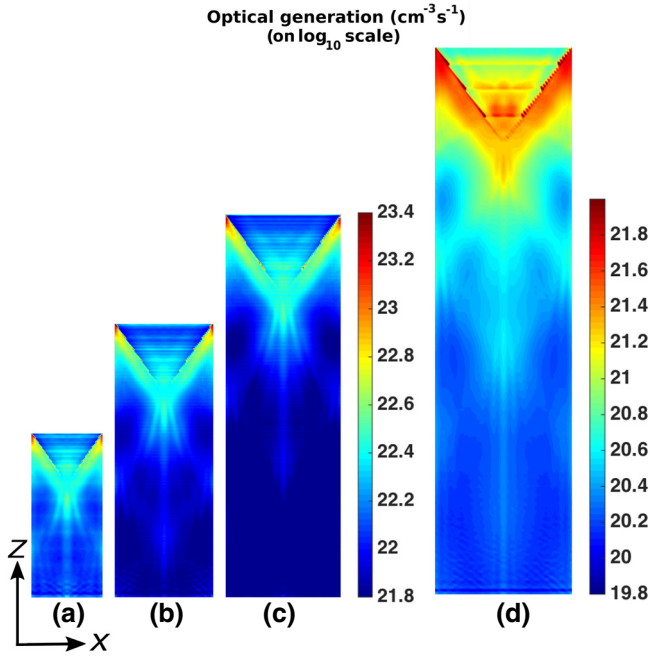


FIG. 5. Carrier-generation rate within the unit cell of various inverted-pyramid-PhC solar cells (integrated along the y direction): (a) $H = 3 \mu\text{m}$, $a = 1300 \text{ nm}$, (b) $H = 5 \mu\text{m}$, $a = 1800 \text{ nm}$, (c) $H = 7 \mu\text{m}$, $a = 2100 \text{ nm}$, and (d) $H = 10 \mu\text{m}$, $a = 2500 \text{ nm}$. The lattice constants correspond to optimized PhCs. In three dimensions, thin wedges of silicon occur within the triangles, leading to carrier generation throughout the 2D regions depicted.

IV. COMPARISON OF LAMBERTIAN AND WAVE-INTERFERENCE-BASED LIGHT TRAPPING

As shown in Table I, the thin-silicon PhC solar cells are able to achieve MAPDs exceeding the upper bounds suggested by statistical ray trapping [12,48]. To gain physical insight into how the light-trapping capability of our optimized PhCs exceeds that of ray optics, we briefly discuss

the underlying assumptions of the Lambertian limit. The geometry associated with the ray-optics picture is depicted in Fig. 7. We assume that the thickness and refractive index of the ray-trapping slab are L and n , respectively. The bottom surface of the slab is assumed to be perfectly reflecting, and the rough top surface has three hypothetical properties: (i) The surface causes no specular reflection of the light rays incident from air. (ii) It allows perfect escape of light from the slab incident at an angle less than the critical angle, θ_c (given by $\sin \theta_c = 1/n$), with respect to surface normal and causes total internal reflection otherwise. Thus, the incident rays within a cone of angle θ_c are allowed to escape. (iii) The surface redirects both the externally incident light and the total internally reflected light randomly at an angle θ with respect to the normal in the slab according to a probability distribution $f(\theta)$. The probability p that the light inside the slab escapes into air is given by the fraction of rays lying within the solid angle formed by the cone of angle θ_c and can be written as

$$p = \int_0^{2\pi} d\phi \int_0^{\theta_c} \sin \theta f(\theta) d\theta. \quad (2)$$

In the case of a Lambertian surface, $f(\theta) = (1/\pi) \cos \theta$, $0 \leq \theta \leq \pi/2$ [49]. For such surfaces, Eq. (2) yields $p = 1/n^2$. From properties (ii) and (iii), rays can undergo multiple bounces within the slab before escaping. Let m be the number of times a ray traverses the distance $2L$ and $G(m)$ be the probability of making m traversals before escaping. Clearly, $G(1) = p$. Also, $G(m) = p(1-p)^{m-1}$ since the ray does not escape in the first $(m-1)$ traversals and finally escapes in the m th traversal. So the average number of traversals is given by $\langle m \rangle = \sum_{m=1}^{\infty} mG(m) = 1/p$. Since the ray is reflected at an angle θ after each total internal reflection, the path length within the slab is given by $2L/\cos \theta$. The average path length in a single traversal

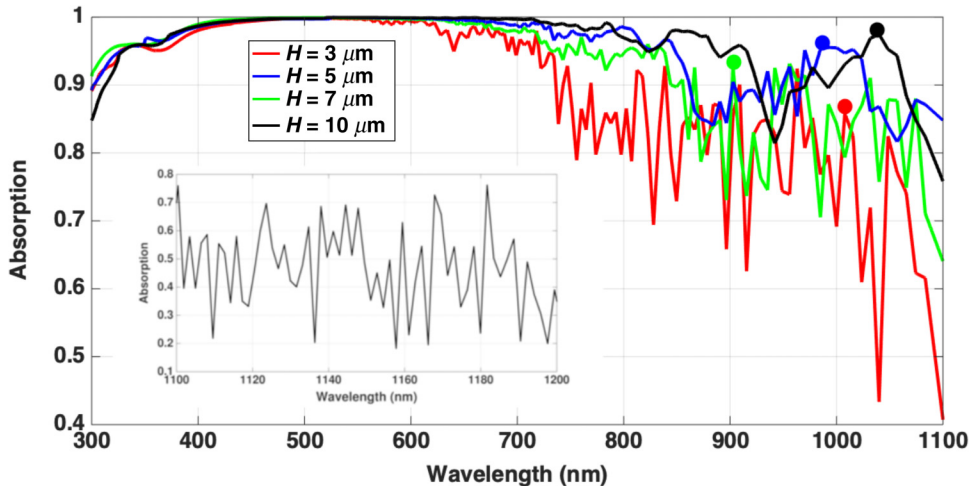


FIG. 6. Absorption spectra of c -Si inverted-pyramid-PhC solar cells with $H = 3, 5, 7,$ and $10 \mu\text{m}$ over the 300–1100-nm wavelength range. The inset shows $1 - R - T$ of the 10- μm PhC over the 1100–1200-nm wavelength range used in computations involving BGN and the Urbach tail. The PhCs are assumed to have the optimized double-layer ARC given in Table I. The solid circles indicate sample resonances with PIR and vortexlike energy flow, shown in Fig. 8.

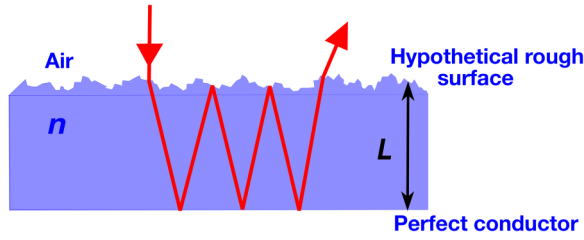


FIG. 7. Statistical ray trapping in a slab with thickness L and refractive index n . Randomly rough, hypothetical top surface with zero specular reflection for all incoming rays and perfect total internal reflection for rays within the slab incident at an angle greater than the critical angle. The slab is placed on a perfect reflector.

can be written as

$$L_{\text{avg}} = \int_0^{2\pi} d\phi \int_0^{\theta_c} \sin \theta f(\theta) \frac{2L}{\cos \theta} d\theta. \quad (3)$$

For a Lambertian surface, the integral in Eq. (3) yields $L_{\text{avg}} = 4L$. Thus, the overall path length can be calculated as $L_{\text{trap}} = L_{\text{avg}}(m) = 4n^2L$, yielding an enhancement factor of $4n^2$. However, PhCs exhibiting PIR modes deviate dramatically from the Lambertian probability distribution and exhibit significant probability of ray propagation close to $\theta = 90^\circ$. Direct numerical solution of Maxwell's equations shows that our PhC structure has multiple parallel-to-interface resonances in the 800–1100-nm wavelength range. Moreover, these slow-light modes with multiple internal bounces and vortexlike energy circulation differ drastically from simple rays of light. PIR and vortexlike modes together increase the effective optical path length by a factor much greater than $4n^2$, yielding a MAPD that exceeds the Lambertian limit. We demonstrate the existence of such resonances and a rich energy-flow pattern within the inverted-pyramid PhC in Figs. 6 and 8.

The solid circles in the absorption spectra in Fig. 6 identify typical resonances that give rise to strong solar-light absorption through coherent light scattering and interference-based effects such as parallel-to-interface and vortexlike propagation of light within the PhC. Figure 8 illustrates such effects for optimized PhCs with $H = 3, 5, 7,$ and $10 \mu\text{m}$ through plots of the in-plane component of the Poynting vector at the resonances marked by solid circles in Fig. 6 ($\lambda = 1008, 902, 986,$ and 1040 nm , respectively). The plot planes in Fig. 8 correspond to the xz slice passing through the center of the PhC unit cell. As shown in Figs. 8(a)–8(c), the 3-, 5-, and 7- μm -thick PhCs exhibit multiple regions with both vortexlike light flow and light flowing purely along the x direction. Figure 8(d) shows that for a 10- μm -thick PhC with an optimum lattice constant of $2.5 \mu\text{m}$, the PIR effect is obscured by the dominant optical vorticity. These PIR and vortexlike

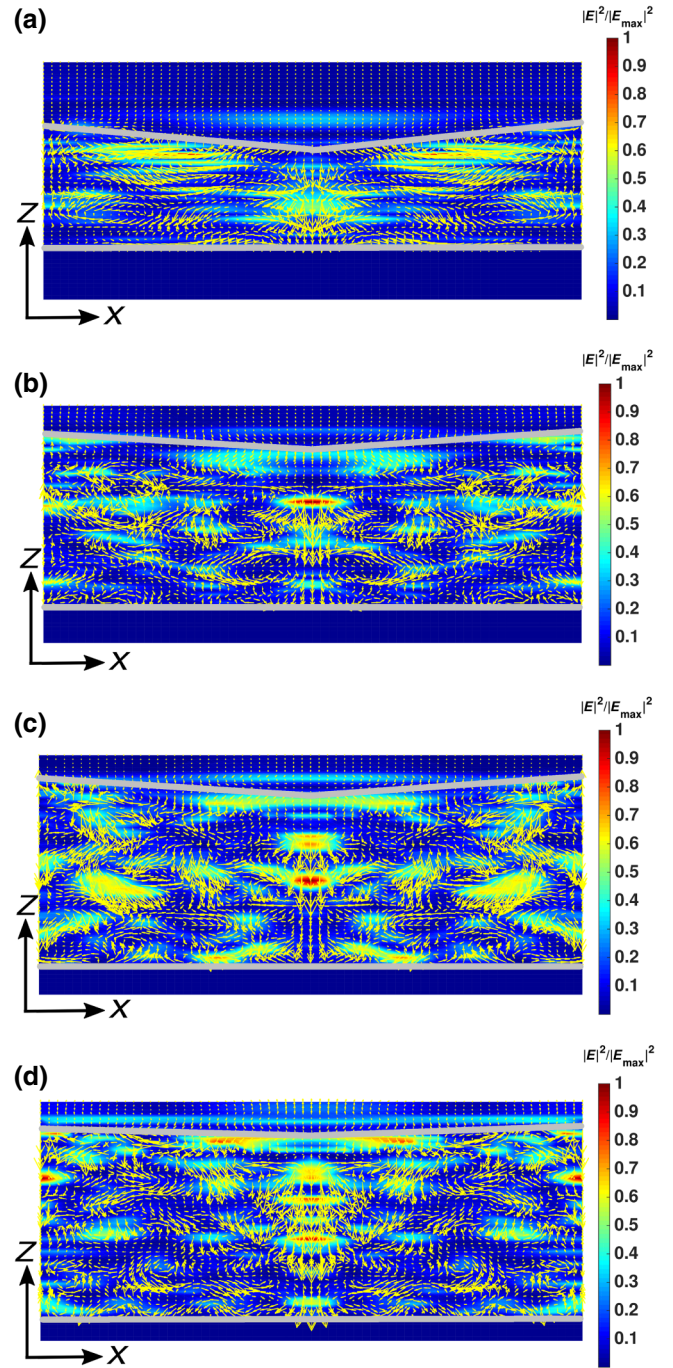


FIG. 8. Parallel-to-interface and vortexlike energy flow in the slow-light modes of the inverted-pyramid PhC. The plot shows in-plane Poynting-vector flow corresponding to the central xz plane of the PhCs: (a) $H = 3 \mu\text{m}$, $\lambda = 1008 \text{ nm}$, (b) $H = 5 \mu\text{m}$, $\lambda = 902 \text{ nm}$, (c) $H = 7 \mu\text{m}$, $\lambda = 986 \text{ nm}$, and (d) $H = 10 \mu\text{m}$, $\lambda = 1040 \text{ nm}$. The color maps show the normalized electric field intensity. The boundary of the c -Si substrate is denoted by a white line. The aspect ratios of the structure is altered to show the Poynting vectors clearly. However, the aspect ratios of the arrows are not altered and their relative lengths at a given point denote the total magnitude of the x and z components of the Poynting vector at that point.

resonances arising from wave interference clearly show that the inverted-micropyramid PhC cannot be accurately described by ray optics.

V. ELECTRONIC OPTIMIZATION

We now analyze the electronic performance of our PhC solar cell using the equivalent carrier-generation profiles obtained through the procedure outlined in Sec. II along with the MAPDs in Table I. With this input generation profile, we optimize the Gaussian doping profiles of the n^+ and p^+ regions that result in the best-possible conversion efficiency of the 10- μm PhC cell.

We first consider the case without BGN [29], in which only optical absorption from the 300–1100-nm range is included. We then consider the more-realistic situation where both BGN and the Urbach optical absorption edge [30–33] contribute to optical generation throughout the entire 300–1200-nm range.

We show that sheet-resistance losses in the highly doped region near the front metallic contacts lead to a slight modification of the doping-profile optimization. For reference, we also include calculations (Appendix A) that do not include this sheet resistance so as to make a direct comparison with previously published hypothetical Lambertian cells [2]. Finally, we present a validation of our 1D transport model by comparing it with exact solutions of the 2D and 3D semiconductor drift-diffusion equations using the exact optical generation profiles obtained from Maxwell’s equations.

A. Sheet resistance

In the top-contact solar cell we consider, photogenerated carriers must flow a considerable lateral distance to reach one of the metallic contact fingers. This lateral flow of current through the narrow emitter results in what is known as “sheet resistance.” This is automatically accounted for in a 2D or 3D transport model. To quantify the effect of

sheet resistance in the simplified 1D transport model, we calculate the power loss (P_{loss}) in the emitter as a fraction of the generated power P_{gen} [51]. We assume initially a top-contact finger spacing of 800 μm as used in the 25%-efficient PERL cell [50]. The actual efficiency of the cell is given by $\eta_{\text{actual}} = \eta (1 - P_{\text{loss}}/P_{\text{gen}})$. The fraction of power lost, $P_{\text{loss}}/P_{\text{gen}}$, due to the sheet resistance can be calculated as [51]

$$\frac{P_{\text{loss}}}{P_{\text{gen}}} = \frac{\rho_{\square} S^2 J_{\text{MP}}}{12 V_{\text{MP}}}, \quad (4)$$

where ρ_{\square} is sheet resistance, S is the distance between emitter grid lines, and J_{MP} and V_{MP} are current density and voltage at the maximum power point of the J - V curve, respectively. The sheet resistances for different N_{f0} and σ_f are calculated with the PV Lighthouse sheet-resistance calculator [52]. Increased emitter width and N_{f0} leads to a lower sheet resistance but results in higher Auger recombination. With use of the 1D transport model, a maximum efficiency of 29.12% is achieved (as shown in Fig. 9) for $N_{f0} = 3 \times 10^{18} \text{ cm}^{-3}$ and $\sigma_f = 205 \text{ nm}$ (equivalently, an emitter width of 730 nm and a sheet resistance of 362 Ω/sq). Overall, these considerations of sheet resistance near the upper contact lead to a very small drop in power conversion efficiency by 0.47% relative to the situation where sheet resistance is ignored (see Appendix A). Our calculations in Appendix B involving 2D and 3D transport models show that this approach provides reasonable agreement with more-microscopic treatments of the same effect.

B. Surface recombination in the 1D transport model

As mentioned in Sec. II, the detailed geometries of the passivation layer, contacts, etc. are subsumed into the front and rear SRVs in the 1D model and appear as boundary conditions for the semiconductor drift-diffusion equations. Since the quality of the contacts and passivation layers

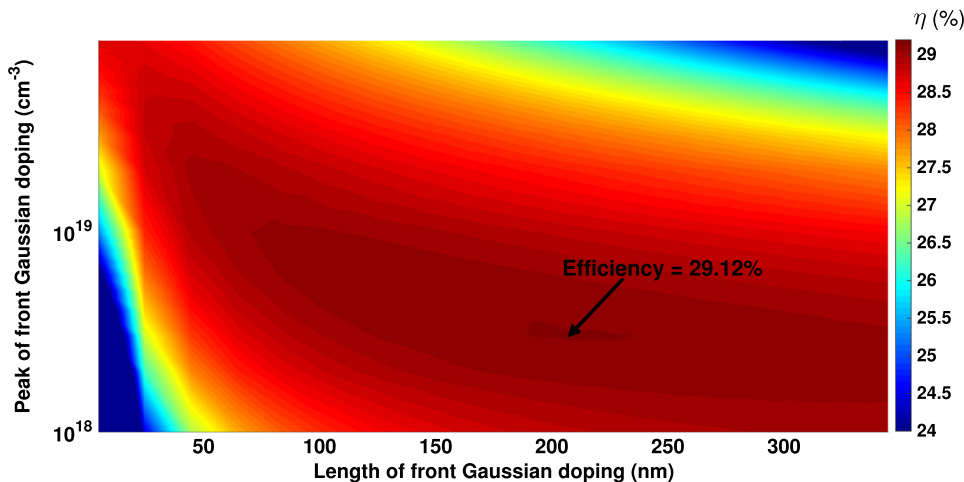


FIG. 9. Emitter optimization including sheet resistance: a maximum efficiency of 29.12% is obtained for $N_{f0} = 3 \times 10^{18} \text{ cm}^{-3}$ and $\sigma_f = 205 \text{ nm}$ (equivalent to an emitter width of 730 nm and sheet resistance of 362 Ω/sq). The finger spacing of the top contact is assumed to be 800 μm (the same as in a 25% PERL cell [50]). Here we assume a MAPD of 42.5 mA/cm^2 arising from solar absorption in the 300–1100-nm wavelength range, $\tau_{\text{SRH}} = 1.2 \text{ ms}$, and temperature of 300 K.

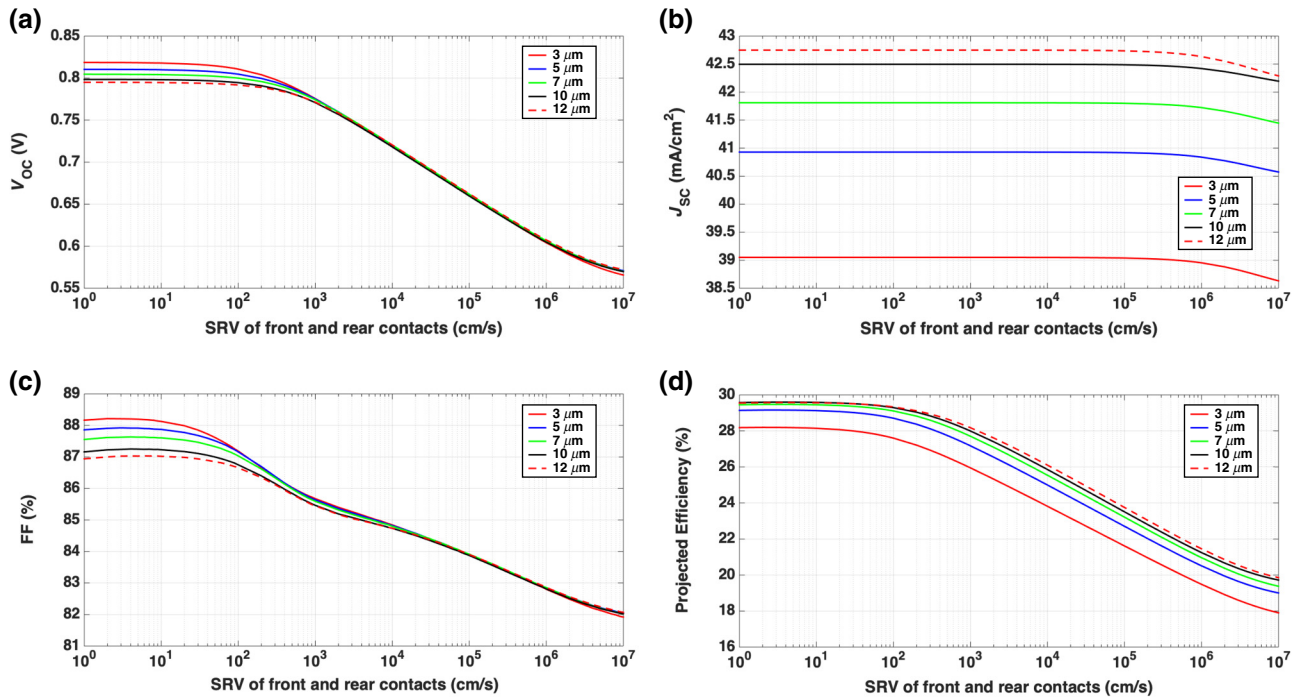


FIG. 10. (a)–(d) Sensitivity of the performance parameters of optimized 3–12 μm -thick, inverted-pyramid-PhC solar cells to changes in SRV of the front and rear contacts (at 27 °C) with optimized n^+pp^+ doping profiles and $\tau_{SRH} = 1.2$ ms. Here solar absorption is restricted to the 300–1100-nm wavelength range and all calculations are performed with a 1D transport model in the absence of sheet resistance. Here the front and back surface fields of the n^+ and p^+ regions considerably mitigate the effects of surface recombination.

affects the performance of the solar cell, we depict in Fig. 10 the variation of the performance parameters of our inverted-micropyramid n^+pp^+ cells with SRVs of the front and rear contacts. The short-circuit current of the n^+pp^+

cell remains constant over a wide range of SRVs due to the strong FSF and BSF of the optimized n^+ and p^+ regions.

An important distinction arises between the solar-cell properties depicted in Fig. 10 for a SRV of more than

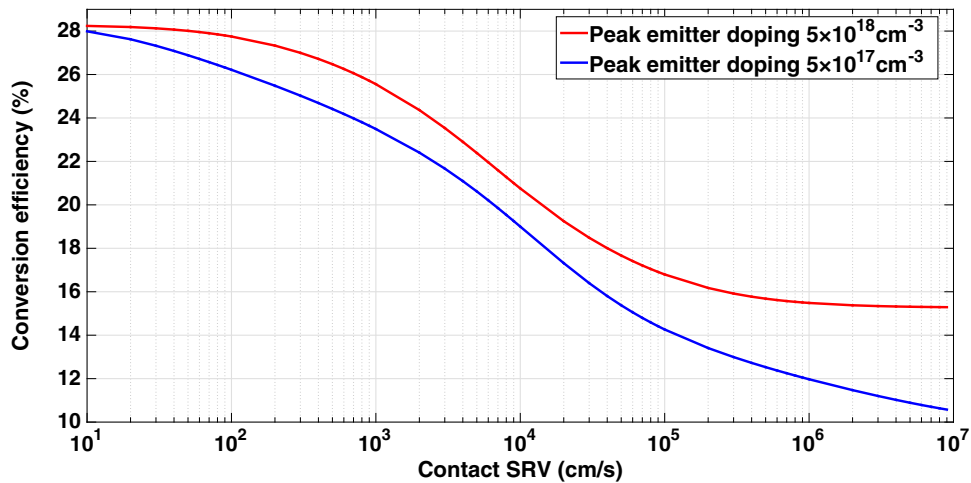


FIG. 11. Dependence of conversion efficiency of a 10 μm -thick n^+p cell on SRV. Red curve: The n^+ emitter has Gaussian doping with a peak concentration of $5 \times 10^{18} \text{ cm}^{-3}$. Blue curve: The peak n^+ doping concentration is $5 \times 10^{17} \text{ cm}^{-3}$ with no back surface field. In both cases, the p -type bulk has a uniform doping concentration of $2 \times 10^{17} \text{ cm}^{-3}$ and the emitter regions are 20 nm thick. The red curve corresponds to the optimum doping shown in Fig. 19. In both cases, the absence of a back surface field leads to more rapid degradation of the efficiency with SRV. For the blue curve, the degradation is more due to nonoptimized emitter doping. For both cases, $\tau_{SRH} = 1.2$ ms and BGN is excluded. Both curves are generated with a 1D transport model before sheet-resistance correction.

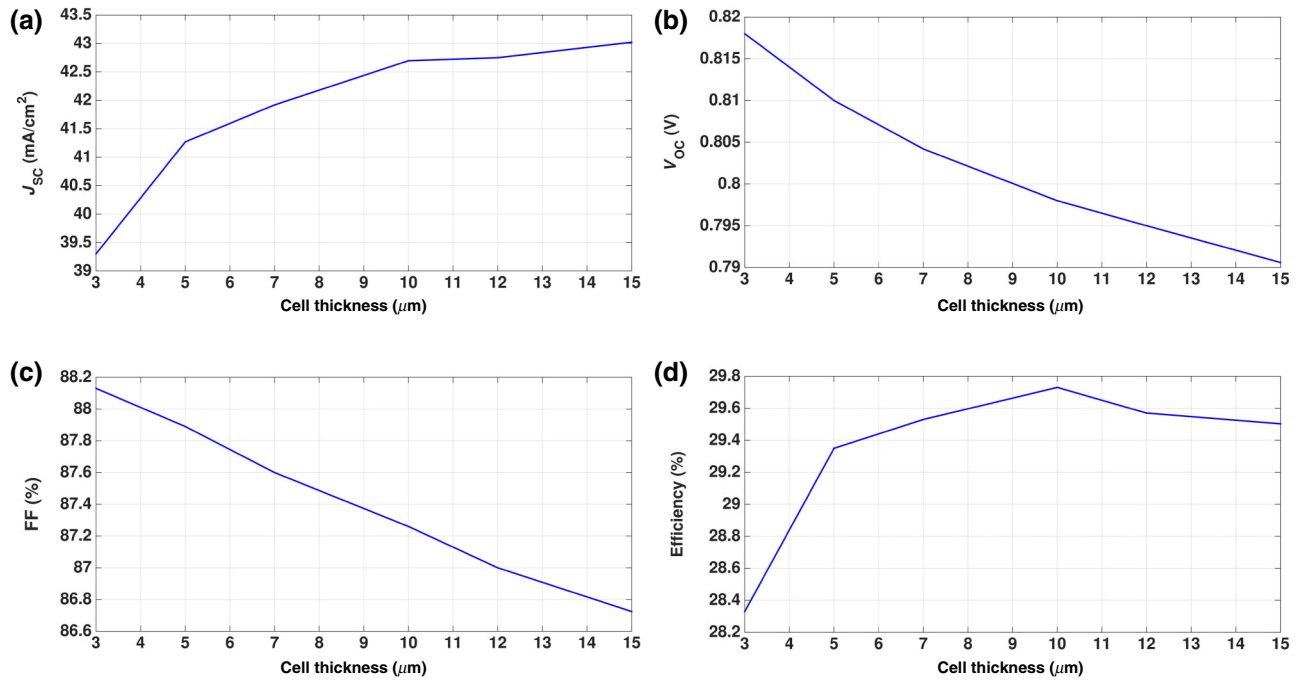


FIG. 12. (a)–(d) Thickness optimization of an inverted-pyramid-PhC solar cell using the optimized n^+pp^+ doping profile and $\tau_{\text{SRH}} = 1.2$ ms at a temperature of 300 K and with solar absorption restricted to the 300–1100-nm wavelength range. These curves are generated with a 1D electronic transport model without sheet-resistance losses.

10^3 cm/s and poorly passivated solar cells. In our case, the FSF and BSF are part of the passivation and offset the effects of the high SRV. In contrast, a poorly passivated cell is represented without a separate FSF or BSF, but all near-surface recombination is described with an overall

effective SRV. The results from such an overall effective SRV are depicted in Fig. 11, where it is seen that solar-cell efficiency degrades much-more dramatically. We fix the p -type uniform bulk doping to 2×10^{17} cm^{-3} (the optimized bulk doping corresponding to Fig. 19). The blue

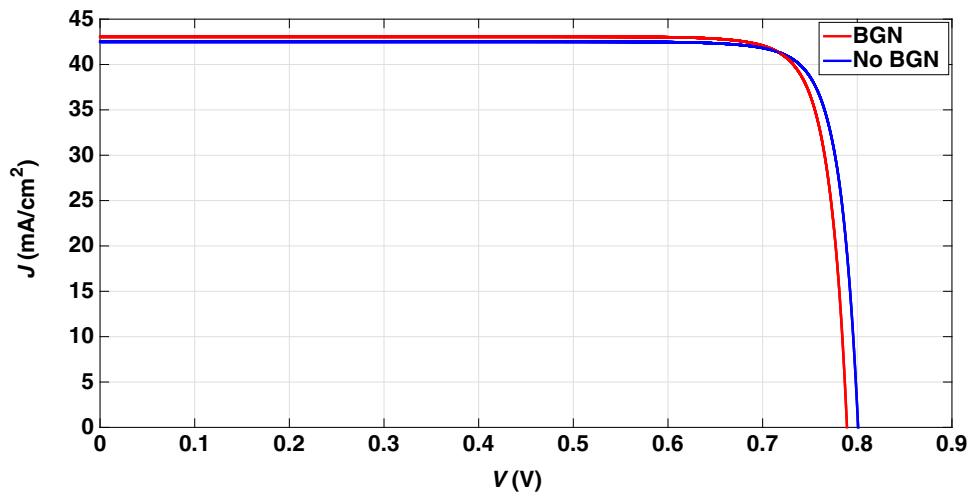


FIG. 13. J - V characteristics of a 10- μm -thick optimized inverted-pyramid-PhC solar cell with and without BGN at a temperature of 25 $^\circ\text{C}$. For the blue curve, solar absorption is restricted to the 300–1100-nm wavelength range, yielding $J_{\text{SC}} = 42.5$ mA/cm^2 , $V_{\text{OC}} = 0.801$ V, a FF of 87.33%, and power conversion efficiency of 29.73%. The red curve includes solar absorption throughout the 300–1200-nm range to include BGN (shift of the continuum edge) and the Urbach tail in c -Si (due to phonon-assisted generation of electron-hole pairs), yielding $J_{\text{SC}} = 43.59$ mA/cm^2 , $V_{\text{OC}} = 0.7894$ V, a FF of 87.25%, and overall power conversion efficiency of 30.02%. In both cases, an optimized n^+pp^+ doping profile is assumed with surface recombination velocities of 10 cm/s and $\tau_{\text{SRH}} = 1.2$ ms. This comparison is obtained in a 1D electronic transport model without sheet-resistance corrections.

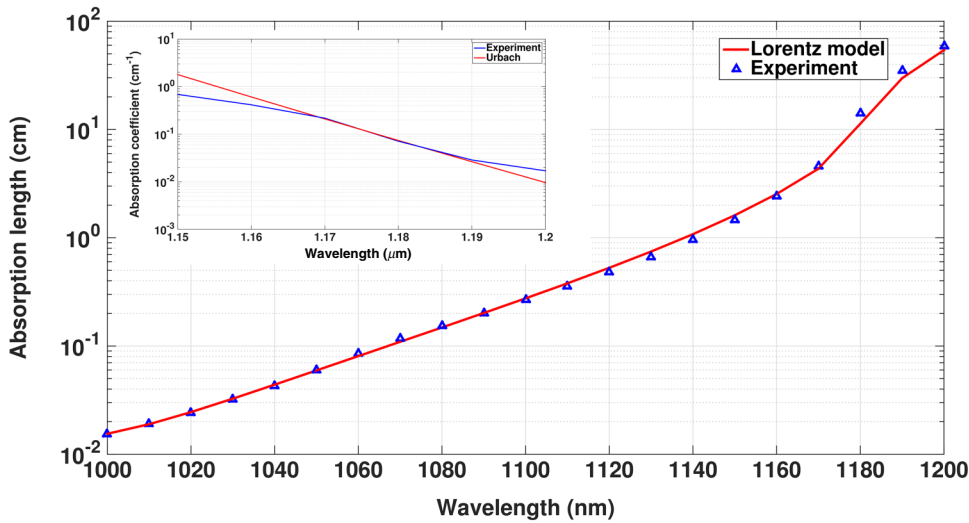


FIG. 14. Comparison of absorption lengths obtained from Ref. [56] and our fitting function with a series of Lorentz oscillator terms (fitting parameters are given in Table II). The inset shows the Urbach slope exhibited by the experimental absorption coefficient from Ref. [56].

curve shows that if a BSF is absent and a nonoptimized FSF doping profile is used, the conversion efficiency degrades more rapidly.

The cells described in Fig. 10 remain under low-level injection at short circuit, leading to very little change in bulk recombination. Under short-circuit conditions, almost all the generated carriers are collected even when the quality of the contact passivation degrades. On the other hand, V_{OC} of the cell remains almost constant only until the front and rear SRVs are 100 cm/s. For thinner cells, both V_{OC} and the fill factor (FF) exhibit relatively faster variation as compared with thicker cells. Overall, for $H \geq 10 \mu\text{m}$, the conversion efficiency of our n^+pp^+ PhC cell exhibits negligible variation with SRV over the range from 1 to 100 cm/s.

C. Cell-thickness optimization

In general, a thicker cell can absorb more light, leading to a higher J_{SC} . On the other hand, increased bulk recombination in a thicker cell leads to a lower V_{OC} . The optimum value of H for maximum conversion efficiency is drastically reduced from that suggested by the Lambertian light-trapping picture. Figures 12(a) and 12(b) show the variation of J_{SC} and V_{OC} with H . As H increases from 3 to 15 μm , V_{OC} decreases from 818.5 to 791 mV. The fill factor exhibits a relatively small drop from 0.882 to 0.867, as seen in Fig. 12(c). As shown in Fig. 12(d), our inverted-micropyramid-PhC solar cell has an optimum thickness of 10 μm with 29.59% power conversion efficiency at 300 K. At 25 $^\circ\text{C}$, our optimum cell, with light bulk doping and heavy doping at the ends, exhibits 29.73% efficiency as compared with a hypothetical 110- μm -thick Lambertian light-trapping cell [2] with 29.57% efficiency at 25 $^\circ\text{C}$. The J - V characteristic of our 29.73%-efficient optimum cell, based on wave-interference light trapping, is shown in Fig. 13 (blue curve). This corresponds to $V_{OC} = 0.801$

V , $J_{SC} = 42.5 \text{ mA/cm}^2$, and a fill factor of 87.33%. In this cell-thickness-optimization study, all the cells are assumed to have optimized MAPD and optimized design parameters as given in Table I.

VI. BAND-GAP NARROWING AND THE URBACH OPTICAL ABSORPTION EDGE

We now consider the effect of BGN in our n^+pp^+ cell. BGN is driven by the excess carrier concentration in our cell, which is large compared with the doping concentration. In Schenk's model [29], BGN is dependent on the total carrier concentration. Using Schenk's model in our SENTAURUS computations, we estimate an approximately-14-meV lowering of the continuum absorption edge. This enables solar absorption for wavelengths as long as 1115 nm in c -Si. For conventional solar cells (without wave-interference-based light trapping), BGN offer little advantage since planar c -Si absorbs negligible sunlight in the long-wavelength range. At the same time, lowering of the optical absorption continuum reduces the open-circuit voltage of the cell. For example, BGN causes a 0.13% efficiency drop in the hypothetical Lambertian solar cell [2]. In contrast, our inverted-micropyramid-PhC solar cell supports wave-interference-based slow-light

TABLE II. Fitting parameters used to fit Si dispersion data of [56].

Wavelength range (nm)	ϵ_∞	$\Delta\epsilon_j$	ω_{pj} ($\times 10^3 \mu\text{m}^{-1}$)	γ_j ($\times 10^3 \mu\text{m}^{-1}$)
1000–1200	1.0	0.971156	0.001805	0.000000
		7.244785	0.006785	0.000001
		0.000580	0.001018	0.000047
		2.519084	0.002291	0.000000
		-0.057262	0.001237	0.000004

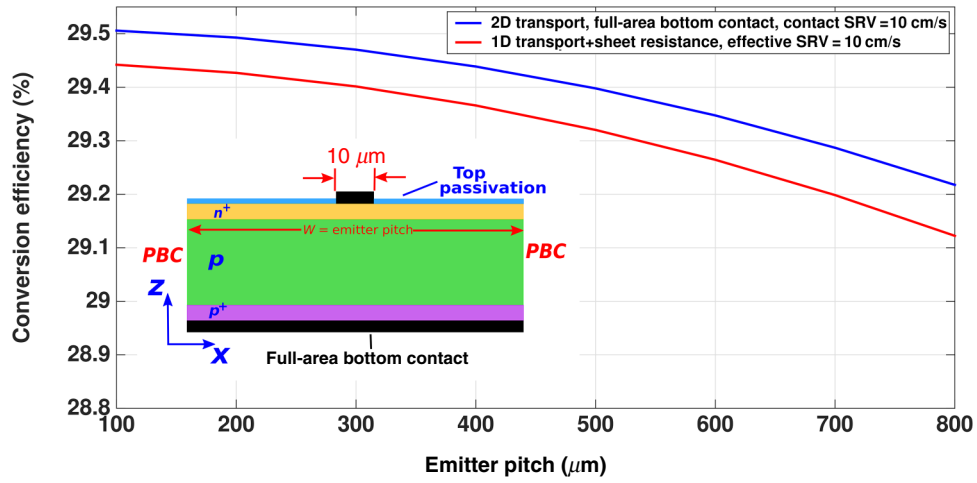


FIG. 15. Effect of sheet resistance and top-contact finger spacing on efficiency (ignoring BGN). Here $\tau_{\text{SRH}} = 1.2$ ms and top-contact fingers are assumed to be cloaked. The blue curve corresponds to the 2D model for the full-area bottom-contact, 10- μm -thick cell. The 730 nm-thick emitter has a Gaussian doping profile with a peak value of $3 \times 10^{18} \text{ cm}^{-3}$. The 200-nm-thick p^+ BSF has a peak doping of $2 \times 10^{19} \text{ cm}^{-3}$. The top contact is 10 μm wide. The uniformly doped p -type bulk has a doping concentration of $5 \times 10^{15} \text{ cm}^{-3}$. The top and bottom contacts are both modeled with an effective SRV of 10 cm/s. The SRV of the insulator-Si interface is determined according to Eq. (B1) with $S_{n0} = 20$ cm/s and $S_{p0} = 1.7$ cm/s. The red curve corresponds to the 1D transport model including sheet resistance. The 1D model has the same doping configurations for the emitter, bulk, and BSF as the 2D cell. The effect of sheet resistance is taken into account according to Eq. (4). The effective SRV for both contacts in the 1D model is 10 cm/s.

modes and other optical resonances [7] in the long-wavelength regime. The incident light is refracted almost parallel to the solar-cell surface, further increasing the path lengths of the long-wavelength photons in the active layer. In the presence of BGN, these trapped photons with a long dwell time are eventually absorbed in c -Si. In our 10- μm -thick n^+pp^+ cell with inverted-pyramid PhCs, a 14-meV band-gap narrowing translates into a 0.27 mA/cm^2 gain in MAPD. On the other hand, external-quantum-efficiency measurements show that c -Si solar cells are capable of collecting carriers generated by light absorption up to 1200 nm [25–28,53,54]. This is more than numerical computations, which suggest absorption up to

approximately 1120 nm based on BGN. Calculations by Zhao *et al.* [25] likewise show a steep cutoff at approximately 1120 nm. This disagreement between the numerical computation and measurement likely stems from the fact that even c -Si exhibits an exponentially decaying Urbach optical absorption edge below the continuum band edge [30,31]. Static disorder in noncrystalline solids is well known to contribute an exponential band tail of localized states below the electronic band edge. However, in c -Si a similar tail of phonon-assisted optical absorption gives rise to electron-hole pairs that are mobile [32,33]. The subgap absorption takes the form of an exponential: $\alpha(\nu) \sim \exp\{[h\nu - E_G(T)/E_0(T)]\}$, where ν is the optical

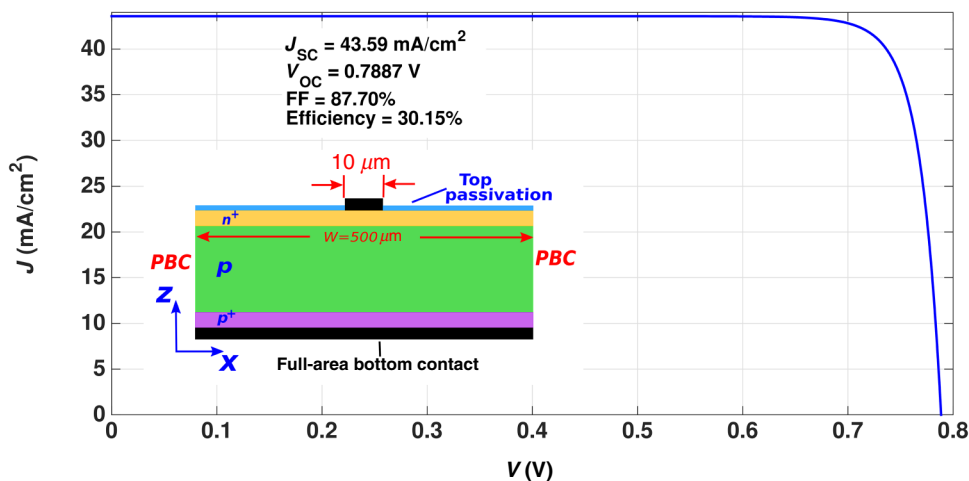


FIG. 16. J - V characteristic, calculated by the 2D transport model, of the full-area bottom-contact cell with BGN, 500- μm emitter pitch, and $\tau_{\text{SRH}} = 10$ ms. The 730-nm-thick emitter of the cell has a Gaussian doping profile with a peak value of $3 \times 10^{18} \text{ cm}^{-3}$. The 200-nm-thick p^+ BSF has a peak doping of $2 \times 10^{19} \text{ cm}^{-3}$. The top contact is 10 μm wide. The contact SRVs of the top and bottom contacts are 10 cm/s. The SRV of the insulator-Si interface is determined according to Eq. (B1) with $S_{n0} = 20$ cm/s and $S_{p0} = 1.7$ cm/s.

TABLE III. Comparison of our thin-silicon inverted-pyramid-PhC solar cells with the hypothetical Lambertian solar cell at 25 °C. The inverted-pyramid-PhC cells use wave-interference-based light trapping. The surface recombination at Si-insulator interfaces of the inverted-pyramid-PhC cells is modeled according to Eq. (B1) with $S_{n0} = 20$ cm/s and $S_{p0} = 1.7$ cm/s. Our 2D transport calculation (which automatically includes the effect of sheet resistance) with BGN, $\tau_{\text{SRH}} = 10$ ms, and 500- μm emitter pitch yields a conversion efficiency of 30.15% for a full-area bottom-contact cell.

Cell type; light-trapping and transport model	Cell thickness (μm)	Bulk recombination model	Surface recombination	V_{OC} (V)	J_{SC} (mA/cm ²)	FF (%)	η (%)
Hypothetical, undoped; perfect Lambertian, no BGN	110	Improved Auger [4], $\tau_{\text{SRH}} = \infty$	No surface recombination	0.7673	43.31	88.98	29.57
Hypothetical, undoped; perfect Lambertian, BGN	110	Improved Auger [4], $\tau_{\text{SRH}} = \infty$	No surface recombination	0.7613	43.31	89.26	29.43
n^+pp^+ inverted-pyramid PhC; no BGN, 2D transport, emitter pitch 800 μm , local-area bottom-contact cell in Fig. 22(a)	10	Improved Auger [4], $\tau_{\text{SRH}} = 1.2$ ms	Top- and bottom-contact SRVs of 10^3 cm/s	0.7975	42.5	85.83	29.09
n^+pp^+ inverted pyramid PhC; BGN, 2D transport, emitter pitch 500 μm , local-area bottom-contact cell in Fig. 22(a)	10	Improved Auger [4], $\tau_{\text{SRH}} = 10$ ms	Top- and bottom-contact SRVs of 10^3 cm/s	0.7815	43.59	87.09	29.8
n^+pp^+ inverted-pyramid PhC; no BGN, 2D transport, emitter pitch 800 μm , full-area bottom-contact cell in Fig. 22(b)	10	Improved Auger [4], $\tau_{\text{SRH}} = 1.2$ ms	Top- and bottom-contact SRVs of 10 cm/s	0.7986	42.5	86.09	29.22
n^+pp^+ inverted-pyramid PhC; BGN, 2D transport, emitter pitch 800 μm , full-area bottom-contact cell in Fig. 22(b)	10	Improved Auger [4], $\tau_{\text{SRH}} = 10$ ms	Top- and bottom-contact SRVs of 10 cm/s	0.7886	43.59	87.07	29.93
n^+pp^+ inverted-pyramid PhC; BGN, 2D transport, emitter pitch 500 μm , full-area bottom-contact cell in Fig. 22(b)	10	Improved Auger [4], $\tau_{\text{SRH}} = 10$ ms	Top- and bottom-contact SRVs of 10 cm/s	0.7887	43.59	87.70	30.15

frequency, $E_G(T)$ is the downshift of the continuum band edge corresponding to BGN, and $E_0(T)$ is the Urbach slope. Cody *et al.* [55] measured the Urbach slope of *c*-Si at 300 K as 8.5 ± 1.0 meV. Microscopic modeling of the optical absorption edge due to both acoustic and optical phonons predicts a slope of 8.6 meV [32,33]. The inset in Fig. 14 shows that the experimental absorption coefficient

from Ref. [56] exhibits an Urbach slope of 8.6 meV over the 1160–1190-nm wavelength range.

To model this behavior, we fit the frequency-dependent dielectric constant of Si over the 1000–1200-nm wavelength range from Ref. [56] to a function of the form $\epsilon(\omega) = \epsilon_\infty + \sum_j \Delta\epsilon_j \omega_{pj}^2 / (\omega_{pj}^2 - 2i\omega\gamma_j - \omega^2)$, where each term of the summation represents a Lorentz

oscillator. The fitting parameters ϵ_∞ , ω_{pj} , $\Delta\epsilon_j$, and γ_j , used in our FDTD computation are obtained with an open MATLAB program [57] and are given in Table II. Figure 14 compares the absorption length ($\lambda/4\pi k$, where k is the imaginary part of the refractive index) obtained from our fit with that calculated from Ref. [56]. The absorption coefficient of the inverted-micropyramid PhC is obtained by high-resolution FDTD calculations in the 1100–1200-nm wavelength range. To ensure convergence of the solutions, the FDTD computations are run for sufficiently long time and the MAPD is finalized only when it shows less than 0.01 mA/cm² variation over 200 FDTD time steps. The inset in Fig. 6 shows a plot of the absorption coefficient for the 10- μ m-thick inverted-micropyramid-PhC solar cell for the 1100–1200-nm spectral range. The optical absorption over the 1115–1200-nm wavelength range corresponds to a MAPD of 0.82 mA/cm². The calculated optical absorption over the 1100–1200-nm wavelength range corresponds to a MAPD of 1.09 mA/cm² (out of the total available 2.93 mA/cm²), leading to the overall $J_{\text{MAPD}} = 43.59$ mA/cm² (300–1200-nm range). The corresponding J - V characteristic is shown by the red curve in Fig. 13. Despite the slight drop of V_{OC} owing to BGN, the conversion efficiency of our optimized 10- μ m-thick inverted-micropyramid-PhC solar cell reaches 30.02%.

VII. SOLAR-CELL-PERFORMANCE PREDICTIONS AND COMPARISON

In this section, we first compare the effect of sheet resistance on the performances of the 1D and 2D models of our 10- μ m-thick inverted-pyramid-PhC cell. For the 2D model, we consider a full-area bottom-contact cell (shown in the inset in Fig. 15) with 10- μ m-wide top contacts. The 730-nm-thick emitter and 200-nm-thick BSF of the 2D cell are assumed to have Gaussian doping profiles with peak doping concentrations of 3×10^{18} and 2×10^{19} cm⁻³, respectively. The p -type bulk has a uniform doping of 5×10^{15} cm⁻³. The SRVs of the top and bottom contacts are both 10 cm/s. The surface recombination at the insulator-Si interface is modeled according to Eq. (B1) with $S_{n0} = 20$ cm/s and $S_{p0} = 1.7$ cm/s. The 1D transport model has the same doping configurations for the emitter, bulk, and BSF as the 2D cell. The contacts of the 1D cell are both assumed to have an effective SRV of 10 cm/s. Figure 15 shows the variation with emitter contact finger pitch of the power conversion efficiencies of the 2D model and 1D transport with the sheet-resistance model [Eq. (4)]. As the contact pitch is decreased from 800 to 200 μ m, the conversion efficiency of the 2D cell increases from 29.22% to 29.49%. Our combined 1D transport and sheet-resistance model captures this trend accurately and predicts the conversion efficiency within an additive factor of 0.1% over the entire range of emitter pitch.

So far, we have used $\tau_{\text{SRH}} = 1.2$ ms in all our simulations. However, measured data (Fig. 5 in Ref. [4]) show that the typical effective lifetime, $\tau_{\text{eff}} = (1/\tau_{\text{SRH}} + 1/\tau_{\text{Aug}})^{-1}$, of p -type samples with a doping concentration of 5×10^{15} cm⁻³ is approximately 10 ms. Since $\tau_{\text{SRH}} > \tau_{\text{eff}}$, it is possible to experimentally obtain $\tau_{\text{SRH}} = 10$ ms. We recalculate the J - V parameters of the full-area bottom-contact cell with an emitter contact pitch of 500 μ m (keeping the doping configurations and SRV models the same) under a more-realistic situation that includes BGN and $\tau_{\text{SRH}} = 10$ ms. Figure 16 shows the corresponding J - V curve of the cell obtained with the 2D transport model with an exact generation profile, which yields 30.15% power conversion efficiency.

The Lambertian-light-trapping-based calculations at 25 °C predict upper bounds for a 10- μ m cell with p -type bulk (doping concentration 5×10^{15} cm⁻³) of $J_{\text{SC}} \sim 39.6$ mA/cm² and $\eta \sim 28.5\%$ (Fig. 4 in Ref. [2]). Compared with the hypothetical Lambertian cell, which ignores the wave nature of light, our inverted-micropyramid PhC with double-layer ARC yields 4 mA/cm² higher J_{SC} and 1.6% (additive) higher conversion efficiency. Table III compares the performance parameters of our realistic PhC cell with the performance predicted for the ideal, undoped Lambertian solar cell [2]. The 110- μ m-thick Lambertian cell is assumed to have perfect AR and no surface recombination.

Table IV lists the amount of solar absorption as the MAPD (column 2) required for various thicknesses, H , of crystalline silicon to achieve 30% power conversion efficiency, with the n^+pp^+ doping configuration, from solar absorption restricted to the 300–1100-nm range. The last

TABLE IV. The second column lists the amount of solar absorption required for various thicknesses, H , of silicon to achieve 30% power conversion efficiency (in the absence of BGN) with wave-interference-based light trapping restricted to the 300–1100-nm wavelength range. This is calculated in the 1D transport model with sheet resistance and 800- μ m top-contact finger spacing with perfect cloaking. Here we take $\tau_{\text{SRH}} = 1.2$ ms. The short-circuit current J_{SC} (essentially the same as MAPD in this case), open-circuit voltage V_{OC} , and FF are then computed with our optimized doping profile. This listed MAPD requirement is reduced if solar absorption in the 1100–1200-nm range is included, τ_{SRH} is increased to 10 ms, a 2D transport model is used, and/or the emitter contact pitch is reduced to 500 μ m.

H (μ m)	Required MAPD (mA/cm ²) for 300–1100-nm wavelength range	V_{OC} (V)	FF (%)
1.6	40.750	0.8318	88.50
3.0	41.348	0.8218	88.27
5.0	41.916	0.8134	87.97
7.0	42.586	0.8045	87.62
10.0	42.862	0.8011	87.35

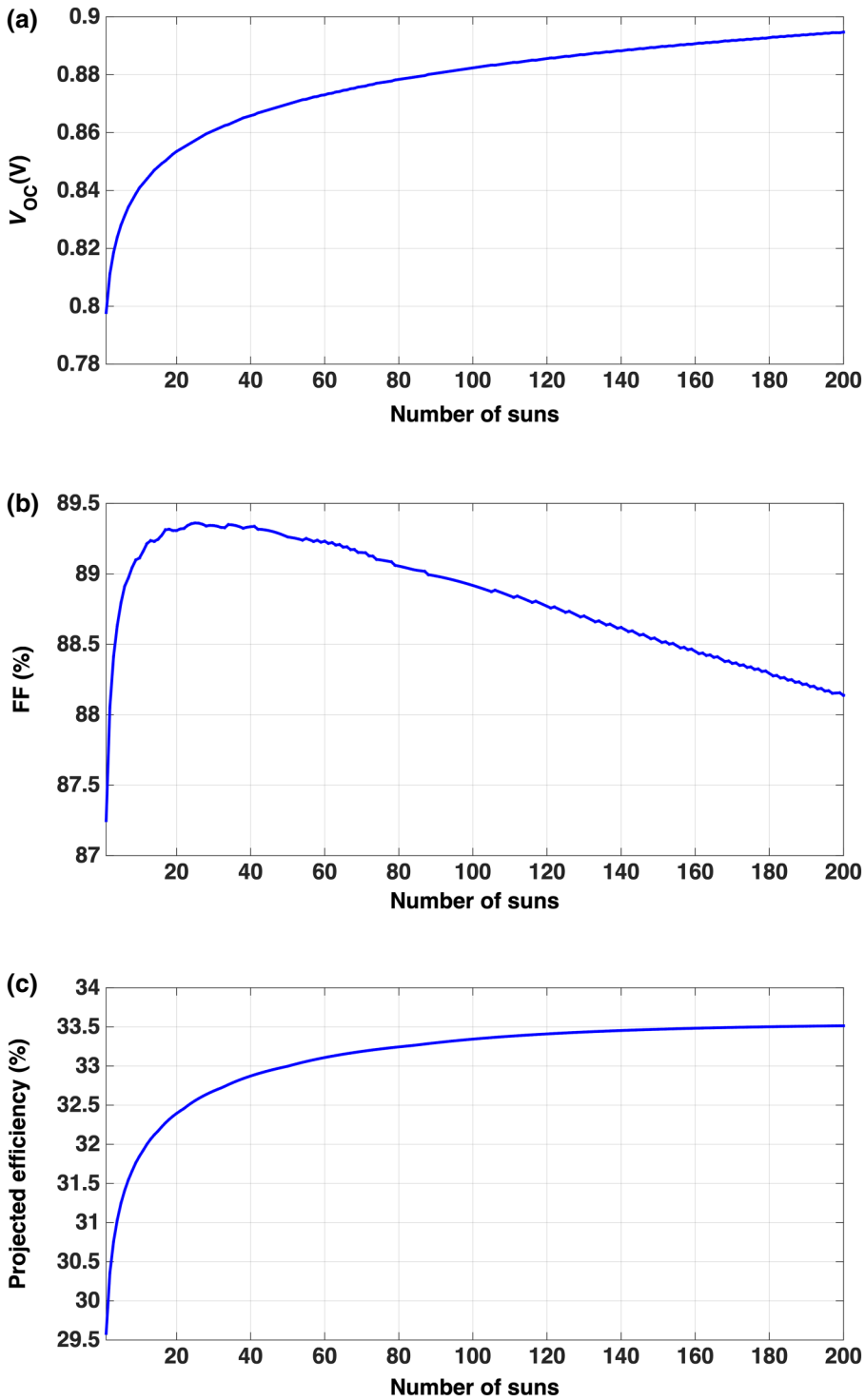


FIG. 17. (a)–(c) Performance of the 10- μm -thick inverted-pyramid-PhC n^+pp^+ cell under solar concentration at 300 K. Here solar absorption is restricted to the 300–1100-nm wavelength range, $\tau_{\text{SRH}} = 1.2$ ms, and the contact SRV is 10 cm/s. The power conversion efficiency saturates to 33.5% at 150-sun illumination. This is obtained in a 1D electronic transport model without sheet resistance.

three columns show the projected values of the short-circuit current, open-circuit voltage, and fill factor that would result in our model if the required solar absorption is achieved. As shown for the 10- μm -thick case, the inclusion of solar absorption in the 1100–1200-nm range, the use of the more-realistic 2D transport model, the increase of τ_{SRH} to 10 ms, or the decrease of the top-contact finger spacing would relax these listed requirements.

We also investigate the performance of our PhC solar cell under solar concentration. With n -sun illumination, the MAPD of the concentrator cell is nJ_{MAPD} . The efficiency is determined by the variation of V_{OC} and the FF with n [plotted in Figs. 17(a) and 17(b), respectively]. For $1 < n \lesssim 20$, V_{OC} increases rapidly due to higher carrier generation. However, the rate of increase of V_{OC} slows for $n > 30$ as very high excess carrier concentration increases

the bulk Auger recombination rate in the cell. On the other hand, the FF of the cell shows a rapid increase up to $n \approx 20$ and then slowly decreases linearly. Figure 17(c) shows that the conversion efficiency of our concentrator cell reaches 32.5% at $n = 20$ and then slowly saturates to 33.5% for $n \geq 150$. A slight increase in these efficiencies is expected with the addition of solar absorption in the 1100–1200-nm range. In this analysis, we assume that the temperature of the cell is maintained at 300 K through a proper cooling mechanism.

VIII. CONCLUSION

In summary, we demonstrate a simple photonic-crystal-solar-cell geometry projected to achieve power conversion efficiency beyond previous theoretical bounds for a single-junction *c*-Si solar cell. This is shown with an inverted-micropyramid PhC that absorbs sunlight beyond the ray-optics-based Lambertian limit through wave-interference-based light trapping. Our FDTD study identifies optimum design parameters for the inverted-pyramid PhC and the double-layer ARC that enables unprecedented MAPDs in very thin (3–12- μm) *c*-Si films owing to long-lifetime photonic resonances in the 800–1200-nm spectral range. The order-of-magnitude reduction of *c*-Si thickness, compared with the hypothetical 110- μm Lambertian cell and world-record-holding 165- μm Kaneka cell, enables our cell to have an unprecedented $V_{\text{OC}} \sim 0.8$ V due to lower bulk recombination. This is the key factor that enables our photonic-crystal solar cell to achieve a projected 30% conversion efficiency. We also demonstrate doping profiles that provide the optimum balance between Auger recombination and the FSF or BSF needed to minimize surface recombination. The resulting electronics is similar to that of a “junctionless” solar cell with carrier-selective contacts [53,54]. The optimum trade-off between solar absorption and bulk recombination yields an optimum thickness for the inverted-pyramid-PhC solar cell of just 10 μm . This represents a paradigm shift from previous beliefs that the optimum thickness for a silicon solar cell should be close to 110 μm [2] or more [5]. In contrast to standard solar panels, our 10- μm -thick silicon photonic-crystal sheets are, in principal, flexible and may be used to conformally coat a variety of surfaces, such as the exterior of buildings.

In addition to describing the optimum situation with $\tau_{\text{SRH}} = 10$ ms, SRVs on the order of 10 cm/s, optimum doping profiles, and ideal contact configurations, we delineate the way in which power conversion efficiency drops if one or more of these conditions is not satisfied. For example, if the surface recombination velocities exceed 100 cm/s, a noticeable reduction in efficiency occurs. If, in addition, the front and back surface fields are not properly engineered, a very-dramatic loss in efficiency arises. A reduction in τ_{SRH} to 1.2 ms typically leads to a

0.5% loss in efficiency. We also show the robustness of our inverted-micropyramid structure to variations in the photonic-crystal lattice constant. *X-Y* symmetry breaking in photonic crystals has been found to be an effective way to further increase solar absorption in thin-film *c*-Si cells [58]. Symmetry breaking of our square-lattice, inverted-micropyramid PhC may likewise enable further improvement in the MAPD over the 300–1200-nm spectral range. Further optimization in wave-interference-based light trapping is still possible. This would effectively compensate for the indirect-band-gap property of *c*-Si and enable it to absorb light as if it were a direct-band-gap semiconductor. A milestone for any single-junction solar cell is the experimental realization of 30% power conversion efficiency. Our study suggests that by including band-gap-narrowing effects, optimizing doping profiles, realizing $\tau_{\text{SRH}} = 10$ ms, keeping surface recombination velocities below 100 cm/s, and using a top-contact (cloaked) finger spacing of 500 μm , the 10- μm -thick *c*-Si photonic-crystal solar cell can achieve this far-reaching goal. The present results provide a useful paradigm for further theoretical and experimental studies of thin-silicon photonic-crystal solar cells combining wave-interference-based solar-light trapping with state-of-the-art electronics.

ACKNOWLEDGMENTS

This work was supported by the U.S. Department of Energy Basic Energy Sciences program in a subcontract under Award No. DE-FGQ2-Q6ER46347.

APPENDIX A

1. Optimization of emitter and BSF

For the sake of comparison with other theoretical models [2], we briefly discuss doping-profile optimization, ignoring sheet resistance losses. In the more-realistic situation that includes sheet resistance for top-contact fingers separated by 800 μm , the optimum thickness of the emitter region is increased. In our 1D model, this causes a lowering of the power conversion efficiency for the optimum doping profile by 0.47%. In the 2D transport model that automatically includes sheet resistance, the efficiency is reduced by 0.37% from the results described below.

Since the n^+ and p^+ regions are very thin compared with the separation between them, the doping profile of one region does not influence the optimum doping profile of the other. Accordingly, we treat the optimizations of these two regions independently. Figures 18(a) and 18(b) show the optimization maps for the front n^+ and rear p^+ regions, respectively. As the widths of the regions with high doping are decreased, the optimum values of the peak doping concentration increase. Also, the optimum conversion efficiency steadily rises as we decrease the widths of the n^+ and p^+ regions (equivalently, as σ_f and σ_r decrease).

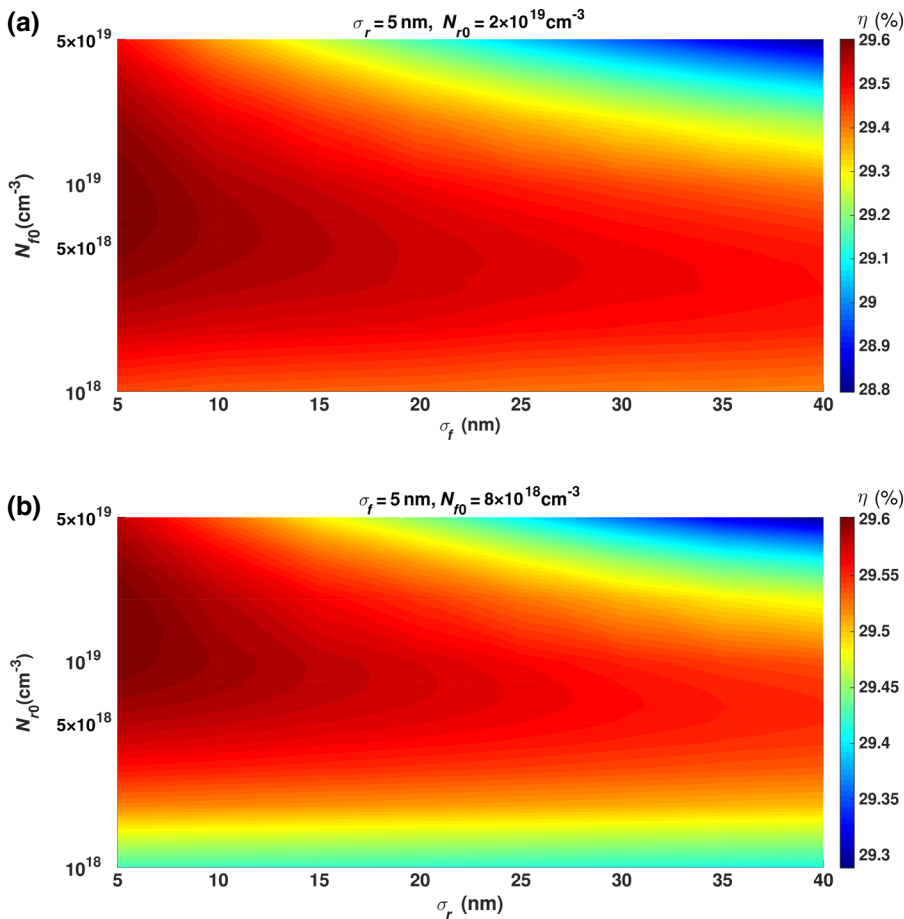


FIG. 18. Optimization maps of Gaussian doping profiles in the 1D transport model with $\tau_{\text{SRH}} = 1.2$ ms and SRV of 10 cm/s, ignoring sheet resistance: (a) front n^+ region (keeping N_{r0} and σ_r fixed) and (b) rear p^+ region (keeping N_{f0} and σ_f fixed). For $\sigma_f = \sigma_r = 5$ nm, the optimum values of N_{f0} and N_{r0} are $8 \times 10^{18} \text{ cm}^{-3}$ and $2 \times 10^{19} \text{ cm}^{-3}$, respectively. The modified optimization map, including sheet resistance, is given in Fig. 9.

This is an artifact of our ignoring sheet resistance. However, a higher doping concentration is necessary for thinner regions to maintain a sufficient FSF or BSF. Higher doping concentrations tend to increase the Auger recombination in the n^+ and p^+ regions. These two competing processes result in optimum N_{f0} and N_{r0} for a given set of σ_f and σ_r . At 300 K, for $\tau_{\text{SRH}} = 1.2$ ms and restricting solar absorption to the 300–1100-nm wavelength range, we obtain the best conversion efficiency of 29.59% for our 10- μm cell with $N_{f0} = 8 \times 10^{18} \text{ cm}^{-3}$, $\sigma_f = 5$ nm, $N_{r0} = 2 \times 10^{19} \text{ cm}^{-3}$, and $\sigma_r = 5$ nm (the corresponding widths of the n^+ and p^+ regions are approximately 20 nm) in comparison with the 29.57% conversion efficiency of the hypothetical Lambertian cell that uses $\tau_{\text{SRH}} \rightarrow \infty$ and ignores surface recombination [2]. Figure 18(a) shows that when σ_r is kept fixed at 5 nm, reduction of σ_f from 35 to 5 nm causes an approximately 0.1% increase in the optimum conversion efficiency. On the other hand, Fig. 18(b) shows that a similar reduction in σ_r (keeping σ_f fixed at 5 nm) increases the conversion efficiency by approximately 0.05%. Thus, the width of the front n^+ layer has a greater influence on the efficiency than that of the rear p^+ layer. In any event, there is a broad range of Gaussian doping profiles for which the power conversion efficiency remains greater than 29%. Our SENTAURUS calculations

with cell thicknesses $H = 3, 5, 7,$ and $12 \mu\text{m}$ reveal that the optimum doping profiles are the same in each case.

2. Comparison with the optimized n^+p solar cell

The classic p - n -junction solar cell with moderately high doping throughout the bulk suffers considerable loss from bulk nonradiative carrier recombination. This is overcome by a profile with low doping throughout the bulk and high-doping n^+ and p^+ regions relegated to thin regions near the top and bottom contacts.

To illustrate the importance of the doping profile, we compare our optimized n^+pp^+ cell with an optimized 10- μm n^+p cell having the same carrier-generation profile. Here we use a 1D transport model, ignoring sheet resistance, assuming $\tau_{\text{SRH}} = 1.2$ ms and SRV of 10 cm/s at both contacts. Figure 19(a) illustrates the doping-profile optimization of the n^+p cell. This shows that the conversion efficiency for the n^+p cell reaches a maximum value of 28.43% for $N_D = 1 \times 10^{19} \text{ cm}^{-3}$ and $N_A = 2 \times 10^{17} \text{ cm}^{-3}$. In Fig. 19(b), we compare the J - V characteristics of both cells. For the n^+p cell, $\eta = 28.43\%$, $J_{\text{SC}} = 42.33 \text{ mA/cm}^2$, $V_{\text{OC}} = 0.782 \text{ V}$, and the FF is 85.86%, whereas for the n^+pp^+ cell, $\eta = 29.59\%$, $J_{\text{SC}} = 42.497 \text{ mA/cm}^2$, $V_{\text{OC}} = 0.798 \text{ V}$, and the FF is 87.23%.

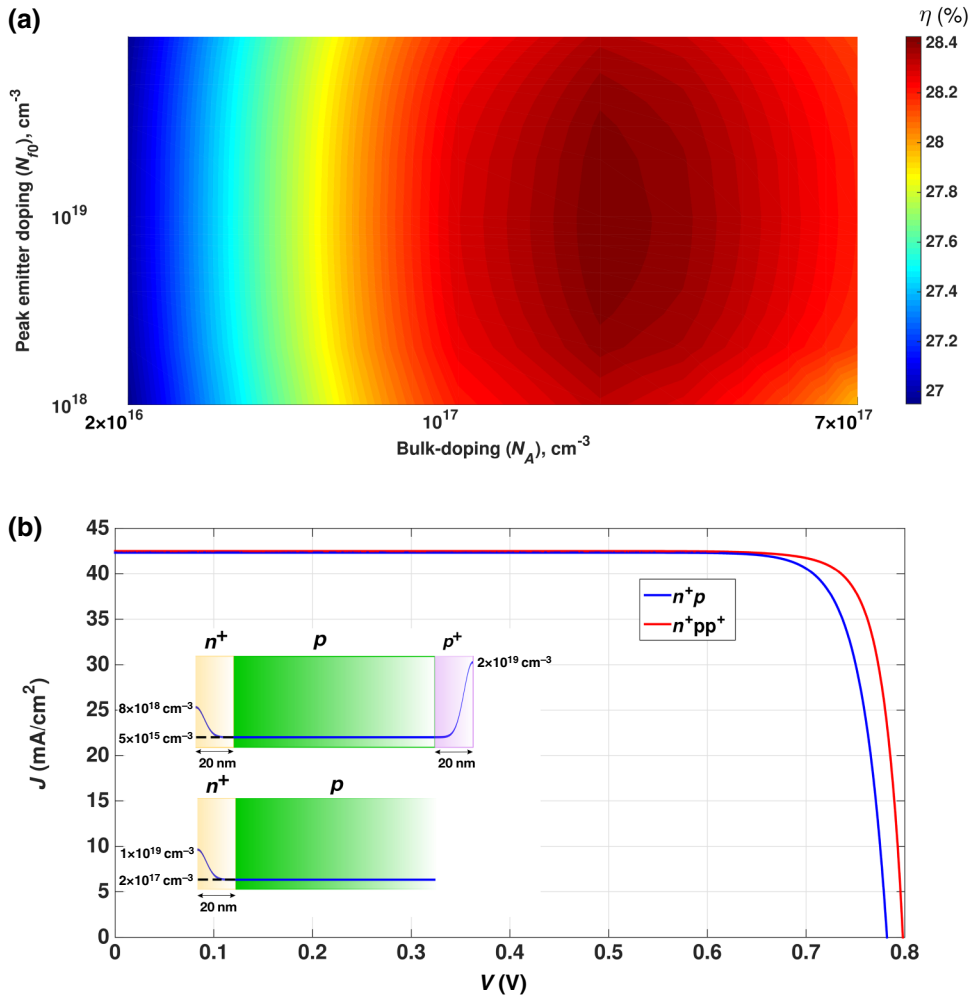


FIG. 19. (a) Doping optimization for an n^+p cell with a 1D transport model, ignoring sheet resistance: the 20-nm n^+ emitter has a Gaussian doping profile and the p -type bulk has uniform doping. (b) Comparison of J - V characteristics of the n^+pp^+ and n^+p cells at 300 K, assuming a MAPD of 42.5 mA/cm² from solar absorption in the 300–1100-nm range. The inset shows the doping profiles used for both cells. In both cases, we assume $\tau_{\text{SRH}} = 1.2$ ms and a SRV of 10 cm/s for top and bottom contacts.

The n^+pp^+ cell has 1.2% higher conversion efficiency due to reduced Auger recombination in the bulk and reduced surface recombination due to the stronger p^+ BSF. The ultrathin architecture of the heavily doped regions helps to minimize Auger recombination in the FSF and BSF regions.

APPENDIX B

1. Comparison of 1D, 2D, and 3D transport models of the $H = 3$ μm cell

As a first step towards validating our 1D transport results, we consider a 3- μm -thick inverted-pyramid-PhC cell. First, we show that for this thin cell, 3D and 2D carrier-transport calculations yield the same results for both low and high values of contact recombination velocities. We also show that the results of the 2D and 3D transport models, which already include the effect of sheet resistance, are in close agreement with our 1D transport model, which separately accounts for sheet resistance through P_{loss} (described in Sec. V). In Appendix B 2, we consider 2D transport calculations for a 10- μm -thick cell and show that the 2D model provides a very slight

enhancement in efficiency relative to the 1D model with sheet resistance. This suggests that essential parameters such as bulk and surface recombination are reasonably taken into account in our 1D transport model through an effective SRV and that actual performance is at least as good as this model predicts. In Appendix B 3, we provide a comparison between actual and equivalent 1D photocarrier-generation profiles. We also compare the efficiencies of full-area back contact and local-area back contact in the 2D transport model.

The optimized 3- μm -thick 3D inverted-pyramid-PhC cell has a lattice constant of 1.3 μm . The conformal n^+ emitter region is 730-nm thick and has a Gaussian doping profile with a peak value of $3 \times 10^{18} \text{ cm}^{-3}$. The full-area, 200-nm-thick p^+ BSF has a Gaussian doping profile with a peak value of $2 \times 10^{19} \text{ cm}^{-3}$. The 3D transport model of the cell includes the effects of the inverted-pyramid texture shown in Fig. 1. The lateral flow of current is calculated and depicted in Fig. 21. For this validation we choose the top-contact and local-area-bottom-contact width as 10 μm . These contacts extend throughout the cell length along y direction. The 2D counterpart of this 3D cell is assumed to have a planar top surface and the same configurations

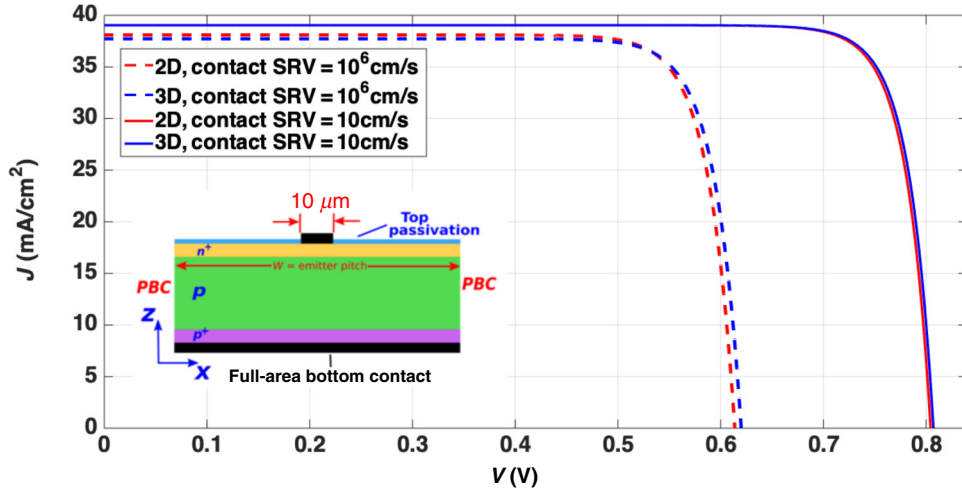


FIG. 20. Two-dimensional and three-dimensional carrier transport calculations for a 3- μm -thick inverted-pyramid-PhC solar cell with $\tau_{\text{SRH}} = 1.2$ ms for low and high surface recombination velocities of the front and rear contacts. The 3D cell is textured with inverted-pyramid-PhCs with a lattice constant of 1.3 μm . The conformal 730-nm-thick emitter has a Gaussian doping profile with a peak value of 3×10^{18} cm^{-3} . The 200-nm-thick p^+ BSF has a peak doping of 2×10^{19} cm^{-3} . The top surface of the 2D cell is assumed to be planar (shown in the inset) and its emitter and BSF have the same configurations as the 3D cell. The unit cell for the 3D transport calculation is 260×260 μm^2 with PBCs along the x direction. The unit cell for the 2D calculation is 260 μm wide with PBCs along the x direction. For the 2D and 3D cases, the top-contact finger width is 10 μm with a pitch of 260 μm .

for doping profiles and contacts (shown in the inset in Fig. 20). The dimensions of the unit cell used in the 3D transport calculation are 260×260 μm^2 (i.e. 200×200 inverted-pyramid-PhC unit cells). PBCs are applied along the x direction for both the 2D model and the 3D model. The 2D counterpart of the 3D model is 260 μm wide. The unit cells for the 2D and 3D transport calculations contain three equidistant base contacts. Thus, the emitter and base-contact pitches are 260 and 86.5 μm , respectively. An equivalent 1D generation profile obtained with the algorithm in Sec. II yields a MAPD of 39.05 mA/cm^2 (as shown in Table I).

For all the 3D and 2D computations, we use SRH statistics for the insulator-Si interface. In this model, the

recombination rate at the Si-insulator interface can be calculated as [59]

$$R_{\text{surface}}^{\text{SRH}} = \frac{(n_s p_s - n_i^2)}{(n_s + n_i)/S_{p0} + (p_s + n_i)/S_{n0}}, \quad (\text{B1})$$

where $S_{j0} = v_{\text{th},j} \sigma_j D_{\text{interface}}$, with $j = n, p$ ($v_{\text{th},j}$ is the thermal velocity, σ_j is the capture cross section, and $D_{\text{interface}}$ is the interface trap density at the oxide-semiconductor interface), n_s and p_s are the electron and hole concentration at the Si surface, and $n_i = \sqrt{N_e N_h} \exp[-E_g(T)/2k_B T]$, where T is the temperature (in kelvins), $E_g(T)$ denotes the band gap of Si, and N_e and N_h are defined in terms of the electron (hole) effective mass m_e^* (m_h^*) and Planck's constant h as $N_j = 2(2\pi m_j^* k_B T/h^2)^{3/2}$ with $j = e$ and h

TABLE V. Comparison of 1D, 2D, and 3D transport models of a 3- μm -thick inverted-pyramid-PhC cell with $\tau_{\text{SRH}} = 1.2$ ms, excluding BGN. The 2D and 3D transport models already include the effect of sheet resistance. The effect of sheet resistance is taken into account in the 1D model through direct calculation of power loss at the maximum power point according to Eq. (4).

Transport model	Contact SRV (cm/s)	J_{SC} (mA/cm^2)	V_{OC} (V)	FF (%)	Fraction of power loss due to sheet resistance (%)	η (%)
1D with sheet resistance	10	39.04 ^a	0.8108 ^a	86.872 ^a	0.1053	27.47
2D	10	39.04	0.8044	86.434	...	27.15
3D	10	39.04	0.8072	86.519	...	27.27
1D with sheet resistance	10^6	38.95 ^a	0.6041 ^a	82.802 ^a	0.0014	19.47
2D	10^6	38.10	0.6138	83.074	...	19.43
3D	10^6	37.73	0.6200	83.213	...	19.47

^aSince this sheet-resistance model does not predict V_{OC} , J_{SC} , or the FF, the corresponding entries are those before the inclusion of sheet-resistance loss.

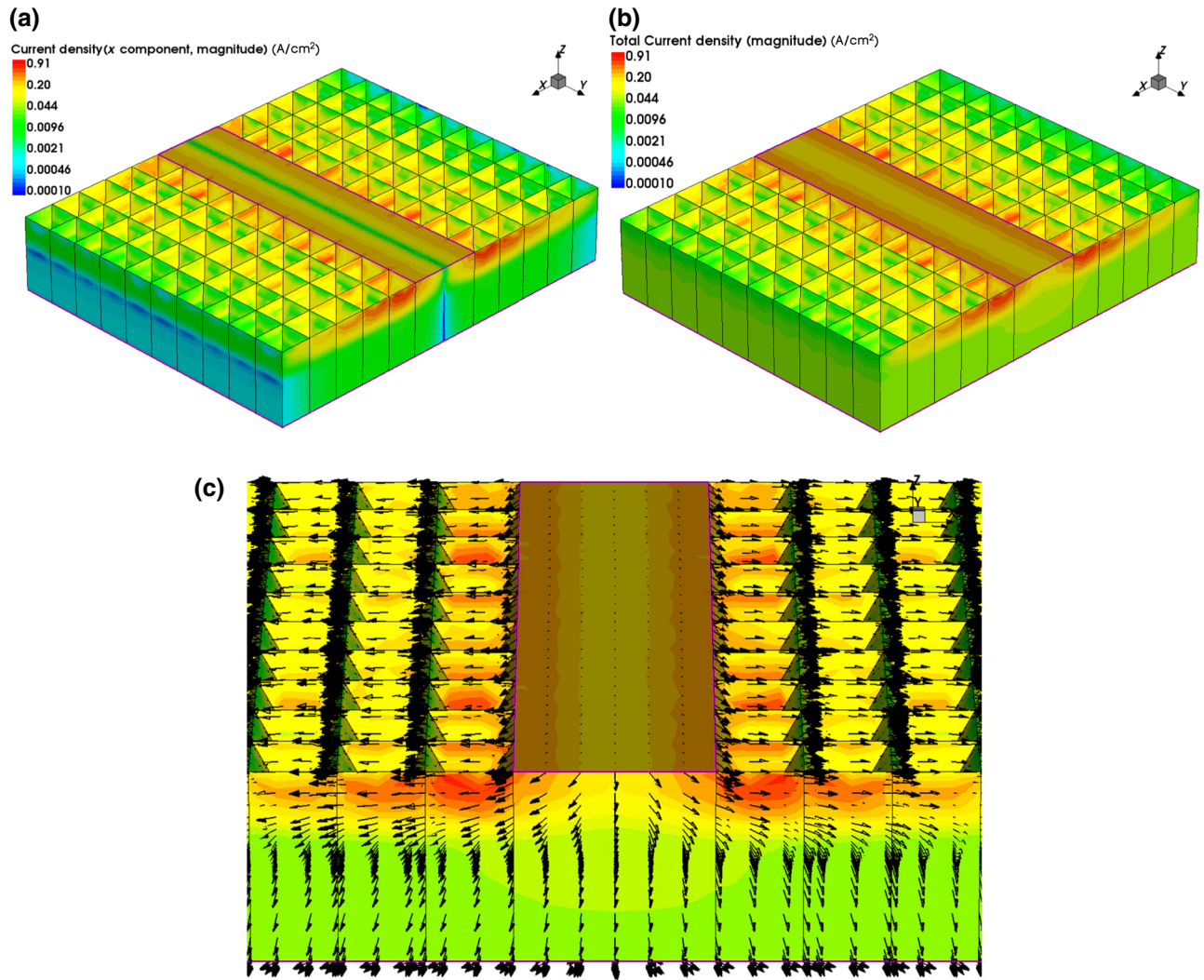


FIG. 21. Three-dimensional carrier transport in a 3- μm -thick inverted-pyramid-PhC solar cell with full-area back contact, $\tau_{\text{SRH}} = 1.2$ ms, and contact SRV of 10 cm/s: (a) magnitude of the x component of the current density and (b) magnitude of the total current density, both plotted at the maximum power point. (c) Plot of the current-density vector field superposed on the total-current-density plot. The flow of negatively charged electrons is opposite to the arrows. (b),(c) have the same scale for the color bar. The 3D cell is textured with inverted-pyramid PhCs with a lattice constant of 1.3 μm . The conformal 730-nm-thick emitter has a Gaussian doping profile with a peak value of $3 \times 10^{18} \text{ cm}^{-3}$. The 200-nm-thick p^+ BSF has a peak doping of $2 \times 10^{19} \text{ cm}^{-3}$. The unit cell for the 3D transport calculation is $260 \times 260 \mu\text{m}^2$ with PBCs along the x and y directions. The top-contact finger width is 10 μm with a pitch of 260 μm . Lateral current flow is very prominent in the vicinity of the textured region near the top as electrons flow towards the top contact.

for electrons and holes, respectively. For electrons, $v_{th} = \sqrt{3k_B T/m_e^*} = 1.12 \times 10^7$ cm/s for $m_e^* = 1.08m_e$ and $T = 298$ K. For holes, v_{th} would be slightly lower due to higher effective mass (approximately $1.5m_e^*$). For the rear oxide surface of a cell with local-area back contacts, the measured value of the near-midgap trap density at the Si-insulator interface, $D_{\text{interface}} = 3 \times 10^9 \text{ cm}^{-2}$ (Table I in Ref. [60]). From the survey of published data on capture cross sections (Fig. 6 in Ref. [61]), $\sigma_p = 6 \times 10^{-17} \text{ cm}^2$ for these traps. The same figure shows that the measured value of σ_n varies over a large range. The choice of $\sigma_n = 6 \times 10^{-16} \text{ cm}^2$ results in an S_{n0} that closely

approximates the effective SRV of the state-of-the-art measurements in Ref. [4]. Accordingly, we choose $S_{n0} \approx 20.16$ cm/s and $S_{p0} \approx 1.7$ cm/s.

For the metal-Si interface, we consider two different cases with effective contact SRVs of 10 and 10^6 cm/s. The J - V curves corresponding to the 2D and 3D models of the 3- μm -thick cell for each choice of contact SRV are shown in Fig. 20. This comparison shows that the 2D and 3D transport models of the 3- μm cell agree well for both good-contact and bad-contact SRVs. For contact SRV of 10 cm/s, the 2D and 3D models yield 27.15% and 27.26% power conversion efficiencies, respectively.

The corresponding values for contact SRV of 10^6 cm/s are 19.47% and 19.43%, respectively. A summary of the 1D, 2D, and 3D transport results for the 3- μm -thick cell in Table V shows that the conversion efficiency predicted by the 1D model with sheet resistance is only 0.2% higher than that predicted by the 3D model for contact SRV = 10 cm/s, whereas for a higher contact SRV, the equivalent 1D model yields the same conversion efficiency as the 3D model. The 1D model is assumed to have the same doping configurations for the bulk, emitter, and BSF as the 2D and 3D cells. In the model, the power loss due to sheet resistance is calculated with Eq. (4) with emitter finger spacing $S = 260$ μm . For the 3D transport calculations, we plot in Fig. 21 the spatial profiles of the current density at the maximum power point of the J - V curve ($V = 0.7283$ V) with contact SRV of 10 cm/s (corresponding to the solid blue J - V curve in Fig. 20). Figure 21(c) shows a plot of the current-density vector field over a volume of the cell. The current near the textured top surface is dominated by its x component. For the rest of the cell, current mainly flows along the z direction.

2. Comparison of 1D and 2D transport models of the $H = 10$ μm cell

In this section, we compare the results of our 1D and 2D transport models for a 10- μm -thick cell with full-area back contact. It is shown that the more-precise 2D transport model predicts an efficiency 0.1% greater than the 1D transport model with sheet resistance separately accounted for.

The geometry of the 2D transport model of the 10- μm -thick inverted-pyramid-PhC cell with full-area back contact is shown in Fig. 22. The dimensions of the unit cell used in our 2D transport calculation are

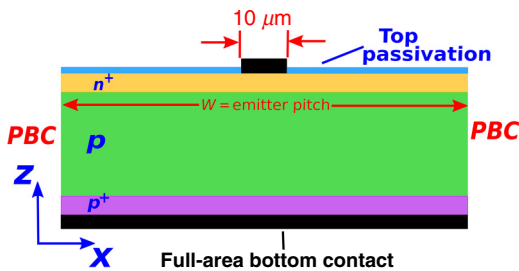


FIG. 22. Two-dimensional transport model of a 10- μm -thick, full-area bottom-contact cell. The 730-nm-thick emitter of the cell has a Gaussian doping profile with a peak value of 3×10^{18} cm^{-3} . The 200-nm-thick p^+ BSF has a peak doping of 2×10^{19} cm^{-3} . The top contact is 10 μm wide. The width (W) of the unit cell for the transport calculation is equal to the emitter pitch, 800 μm . The contact SRVs of the top and bottom contacts are 10 cm/s. The SRV of the insulator-Si interface is determined according to Eq. (B1) with $S_{n0} = 20$ cm/s and $S_{p0} = 1.7$ cm/s. Here we choose $\tau_{\text{SRH}} = 1.2$ ms.

determined by the emitter pitch. We apply PBCs along the x direction. The cell uses a 730 nm-thick emitter and a 200 nm-thick p^+ BSF with Gaussian doping profiles. The peak doping concentrations for the emitter and the BSF are 3×10^{18} and 2×10^{19} cm^{-3} , respectively. The bulk p region has a uniform doping concentration of 5×10^{15} cm^{-3} . The top-contact width is 10 μm . The contact SRVs for the top and bottom contacts are both assumed to be 10 cm/s. The carrier recombination at the Si-insulator surface is described according to the SRH model of Eq. (B1) with $S_{n0} = 20$ cm/s and $S_{p0} = 1.7$ cm/s. For a fixed emitter contact finger pitch of 800 μm , we compare the J - V parameters of the 2D and 1D models in Table VI. Our 1D equivalent model with an effective SRV of 10 cm/s, along with the sheet resistance loss (according to Eq. (4)), underestimates the efficiency of the 2D model by an additive factor of 0.1%.

3. Local-area back-contact cell

We consider an alternative 2D cell geometry with local-area back contacts in Fig. 23. The emitter contact finger pitch is 800 μm , whereas the bottom-contact pitch is 266.5 μm . The 2D transport calculation is performed with PBCs and a unit cell consisting of 320 photonic-crystal unit cells, spanning 800 μm . The top and bottom contacts are both 10 μm wide and have SRVs of 1000 cm/s. The 730-nm-thick emitter of the cell has a Gaussian doping profile with a peak value of 3×10^{18} cm^{-3} . The 200-nm-thick p^+ BSF has a peak doping of 2×10^{19} cm^{-3} . The SRV of the insulator-Si interface is determined according to Eq. (B1) with $S_{n0} = 20$ cm/s and $S_{p0} = 1.7$ cm/s. We choose $\tau_{\text{SRH}} = 1.2$ ms. The J - V parameters of this cell from Table VI illustrate that it is possible to have a higher contact SRV and still design a cell that is able to achieve similar conversion

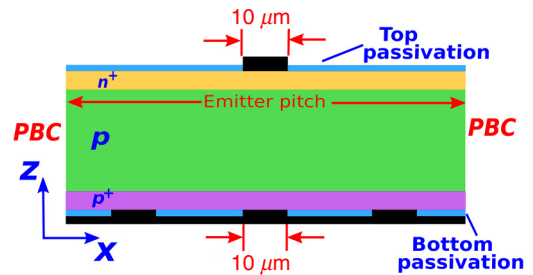


FIG. 23. Two-dimensional transport model of a 10- μm -thick, local-area bottom-contact cell. The unit cell for the transport calculation is 800 μm wide and has one top contact and three equidistant bottom contacts. The top and bottom contacts are 10 μm wide and have SRVs of 1000 cm/s. The 730-nm-thick emitter of the cell has a Gaussian doping profile with a peak value of 3×10^{18} cm^{-3} . The 200-nm-thick p^+ BSF has a peak doping of 2×10^{19} cm^{-3} . The SRV of the insulator-Si interface is determined according to Eq. (B1) with $S_{n0} = 20$ cm/s and $S_{p0} = 1.7$ cm/s. Here $\tau_{\text{SRH}} = 1.2$ ms.

TABLE VI. Comparison of 2D and 1D transport models for the 10- μm -thick cell with $\tau_{\text{SRH}} = 1.2$ ms excluding BGN. The power loss in the 1D model due to sheet resistance is accounted for with Eq. (4). The J - V parameters, obtained with the actual integrated generation profile, are found to be the same as those obtained with the equivalent generation profile (calculated according to the algorithm described in Sec. II). Both full-area and local-area bottom-contact configurations are found to be in reasonable agreement with the 1D transport model that takes into account sheet resistance.

Transport model	Contact SRV (cm/s)	J_{SC} (mA/cm ²)	V_{OC} (V)	FF (%)	Fraction of power loss due to sheet resistance (%)	η (%)
1D, with sheet resistance, equivalent generation profile	10	42.5 ^a	0.7998 ^a	87.402 ^a	1.103	29.12
2D, full-area bottom contact, equivalent generation profile	10	42.5	0.7986	86.085	...	29.22
2D, local-area bottom contact, equivalent generation profile	10 ³	42.5	0.7975	85.831	...	29.09
2D, local-area bottom contact, actual generation profile	10 ³	42.5	0.7975	85.827	...	29.09

^aSince this sheet-resistance model directly calculates the power loss at the maximum power point and does not predict V_{OC} , J_{SC} , or the FF, the corresponding entries are those before the inclusion of sheet-resistance loss.

efficiency as our full-area back-contact 2D model and 1D model.

The last two rows in Table VI compare the performance parameters of the local-area bottom-contact cell obtained with the equivalent carrier-generation profile (calculated according to the algorithm described in Sec. II) with those obtained with the actual integrated carrier-generation profile in Fig. 5(e). The carrier-generation rate is repeated over 320 unit cells of the PhC to cover the 800- μm separation of the 10- μm -wide front contacts. The performance parameters corresponding to both carrier-generation profiles show excellent agreement, both yielding a power conversion efficiency of 29.09%.

- [1] W. Shockley and H. J. Queisser, Detailed balance limit of efficiency of p-n junction solar cells, *J. Appl. Phys.* **32**, 510 (1961).
- [2] A. Richter, M. Hermle, and S. W. Glunz, Reassessment of the limiting efficiency for crystalline silicon solar cells, *IEEE J. Photovoltaics* **3**, 1184 (2013).
- [3] T. Tiedje, E. Yablonovitch, G. Cody, and B. Brooks, Limiting efficiency of silicon solar cells, *IEEE Trans. Electron Devices* **31**, 711 (1984).
- [4] A. Richter, S. W. Glunz, F. Werner, J. Schmidt, and A. Cuevas, Improved quantitative description of Auger recombination in crystalline silicon, *Phys. Rev. B* **86**, 165202 (2012).
- [5] K. Yoshikawa, H. Kawasaki, W. Yoshida, T. Irie, K. Konishi, K. Nakano, T. Uto, D. Adachi, M. Kanematsu, H.

Uzu, and K. Yamamoto, Silicon Heterojunction solar cell with interdigitated back contacts for a photoconversion efficiency over 26%, *Nat. Energy* **2**, 17032 (2017).

- [6] M. A. Green, Y. Hishikawa, E. D. Dunlop, D. H. Levi, J. Hohl-Ebinger, and A. W. Y. Ho-Baillie, Solar cell efficiency tables (version 51), *Prog. Photovolt. Res. Appl.* **26**, 3 (2018).
- [7] A. Chutinan and S. John, Light trapping and absorption optimization in certain thin-film photonic crystal architectures, *Phys. Rev. A* **78**, 023825 (2008).
- [8] S. John, Strong localization of photons in certain disordered dielectric superlattices, *Phys Rev. Lett* **58**, 2486 (1987).
- [9] E. Yablonovitch, Inhibited Spontaneous Emission in Solid-state Physics and Electronics, *Phys. Rev. Lett.* **58**, 2059 (1987).
- [10] G. Demsey and S. John, Solar energy trapping with modulated silicon nanowire photonic crystals, *J. Appl. Phys.* **112**, 074326 (2012).
- [11] A. Deinega and S. John, Solar power conversion efficiency in modulated silicon nanowire photonic crystals, *J. Appl. Phys.* **112**, 074327 (2012).
- [12] S. Eyderman, S. John, and A. Deinega, Solar light trapping in slanted conical-pore photonic crystals: Beyond statistical ray trapping, *J. Appl. Phys.* **113**, 154315 (2013).
- [13] S. Eyderman, S. John, M. Hafez, S. S. Al-Ameer, T. S. Al-Harby, Y. Al-Hadeethi, and D. M. Bouwes, Light-trapping optimization in wet-etched silicon photonic crystal solar cells, *J. Appl. Phys.* **118**, 023103 (2015).
- [14] A. Mavrokefalos, S. E. Han, S. Yerci, M. S. Branham, and G. Chen, Efficient light trapping in inverted nanopyramid thin crystalline silicon membranes for solar cell applications, *Nano Lett.* **12**, 2792 (2012).

- [15] M. S. Branham, W. Hsu, S. Yerci, J. Loomis, S. V. Boriskina, B. R. Hoard, S. E. Han, and G. Chen, 15.7% efficient 10- μm -thick crystalline silicon solar cells using periodic nanostructures, *Adv. Mater.* **27**, 2182 (2015).
- [16] K. Kumar, A. Khalatpour, G. Liu, J. Nogami, and N. P. Kherani, Converging photo-absorption limit in periodically textured ultra-thin silicon foils and wafers, *Sol. Energy* **15**, 1306 (2017).
- [17] P. Kuang, S. Eyderman, M. L. Hsieh, A. Post, S. John, and S. Y. Lin, Achieving an accurate surface profile of a photonic crystal for near-unity solar absorption in a super thin-film architecture, *ACS Nano* **10**, 6116 (2016).
- [18] M. Ernst and R. Brendel, Lambertian light trapping in thin macroporous silicon layers, *Phys. Status Solidi RRL* **8**, 235 (2014).
- [19] A. Bozzola, M. Liscidini, and L. C. Andreani, Photonic light-trapping versus Lambertian limits in thin film silicon solar cells with 1D and 2D periodic patterns, *Opt. Express* **20**, A224 (2012).
- [20] Z. Yu, A. Raman, and S. Fan, Fundamental limit of nanophotonic light trapping in solar cells, *PNAS* **107**, 17491 (2010).
- [21] L. A. Weinstein, W. C. Hsu, S. Yerci, S. Boriskina, and G. Chen, Enhanced absorption of thin-film photovoltaic cells using an optical cavity, *J. Opt.* **17**, 055901 (2015).
- [22] I. Valuev, A. Deinega, A. Knizhnik, and B. Potapkin, Creating numerically efficient FDTD simulations using generic C++ programming, *Lect. Notes Comput. Sci.* **4707**, 213 (2007).
- [23] P. Campbell and M. A. Green, Light trapping properties of pyramidally textured surfaces, *J. Appl. Phys.* **62**, 243 (1987).
- [24] J. Zhao, A. Wang, and M. A. Green, 24.5% efficiency silicon PERT cells on MCZ substrates and 24.7% efficiency PERL cells on FZ substrates, *Prog. Photovolt: Res. Appl.* **7**, 471 (1999).
- [25] J. Zhao and A. Wang, Rear emitter n -type passivated emitter, rear totally diffused silicon solar cell structure, *Appl. Phys. Lett.* **88**, 242102 (2006).
- [26] J. Benick, B. Steinhauser, R. Muller, J. Bartsch, M. Kamp, A. Mondon, A. Richter, M. Hermle, and S. Glunz, in Proc. of 40th Photovoltaic Specialist Conference (PVSC), 3637 (2014).
- [27] W. Cai, S. Yuan, Y. Sheng, W. Duan, Z. Wang, Y. Chen, Y. Yang, P. P. Altermatt, P. J. Verlinden, and Z. Feng, 22.2% efficiency n -type PERT solar cell, *Energy Procedia* **92**, 399 (2016).
- [28] F. Kiefer, J. Krugener, F. Heinemeyer, M. Jestremski, H. J. Osten, R. Brendel, and R. Peibst, Bifacial, fully screen-printed n -PERT solar cells with BF_2 and B implanted emitters, *Sol. Energy Mater. Sol. Cells* **157**, 326 (2016).
- [29] A. Schenk, Finite-temperature full random-phase approximation model of band gap narrowing for silicon device simulation, *J. Appl. Phys.* **84**, 3684 (1998).
- [30] F. Urbach, The long-wavelength edge of photographic sensitivity and of the electronic absorption of solids, *Phys. Rev.* **92**, 1324 (1953).
- [31] W. Martienssen, The optical absorption edge in ionic crystals, *Phys. Chem. Solids* **2**, 257 (1957).
- [32] C. H. Grein and S. John, Temperature dependence of the fundamental optical absorption edge in crystals and disordered semiconductors, *Solid State Commun.* **70**, 87 (1989).
- [33] C. H. Grein and S. John, Temperature dependence of the Urbach optical absorption edge: A theory of multiple phonon absorption and emission sidebands, *Phys. Rev. B* **39**, 1140 (1989).
- [34] M. F. Schumann, S. Wiesendanger, J. C. Goldschmidt, B. Blasi, K. Bittkau, U. W. Paetzold, A. Sprafke, R. B. Wehrspohn, C. Rockstuhl, and M. Wegener, Cloaked contact grids on solar cells by coordinate transformations: Designs and prototypes, *Optica* **2**, 850 (2015).
- [35] M. Langenhorst, M. F. Schumann, R. Schmager, J. Lehr, U. Lemmer, M. Wegener, B. Richards, and U. W. Paetzold, Performance of silicon solar cells with cloaked contact fingers under realistic conditions, Light, Energy and the Environment, OSA Technical Digest (online), PW2A.3 (2017).
- [36] M. F. Schumann, M. Langenhorst, M. Smeets, K. Ding, U. W. Paetzold, and M. Wegener, All-angle invisibility cloaking of contact fingers on solar cells by refractive free-form surfaces, *Adv. Opt. Mater.* **5**, 1700164 (2017).
- [37] E. S. Roman, A. Vitrey, J. Buencuerpo, I. Prieto, J. M. Llorens, A. Garcia-Martin, B. Alen, A. Chaudhuri, A. Neumann, S. R. J. Brueck, and J. M. Ripalda, Cloaking of solar cell contacts at the onset of Rayleigh scattering, *Sci. Rep.*, **6**, 28669 (2016).
- [38] <http://fdtd.kintechlab.com/en/download>
- [39] A. Deinega and S. John, Effective optical response of silicon to sunlight in the finite-difference time-domain method, *Opt. Lett.* **37**, 112 (2012).
- [40] Synopsys, Synopsys TCAD, release M-2016.12 (2016).
- [41] J. Zhao, A. Wang, P. Campbell, and M. A. Green, 22.7% Efficient silicon photovoltaic modules with textured front surface, *IEEE Trans. Electron. Dev.* **46**, 1495 (1999).
- [42] H. Y. Chen et al., Enhanced performance of solar cells with optimized surface recombination and efficient photon capturing via anisotropic-etching of black silicon, *Appl. Phys. Lett.* **104**, 193904 (2014).
- [43] M. F. Abdullah, M. A. Alghoul, H. Naser, N. Asim, S. Ahmadi, B. Yatim, and K. Sopian, Research and development efforts on texturization to reduce the optical losses at front surface of silicon solar cell, *Renew. Sust. Energy Rev.* **66**, 380 (2016).
- [44] N. Borojevic, A. Lennon, and S. Wenham, Light trapping structures for silicon solar cells via inkjet printing, *Phys. Status Solidi A* **211**, 1617 (2014).
- [45] H. Y. Chen, H. L. Lu, Q. H. Ren, Y. Zhang, X. F. Yang, S. J. Ding, and D. W. Zhang, Enhanced photovoltaic performance of inverted pyramid-based nanostructured black-silicon solar cells passivated by an atomic-layer deposited Al_2O_3 layer, *Nanoscale* **7**, 15142 (2015).
- [46] O. Hohn, N. Tucher, and B. Blasi, Theoretical study of pyramid sizes and scattering effects in silicon photovoltaic module stacks, *Opt. Express* **26**, A320 (2018).
- [47] K. Q. Le and S. John, Synergistic plasmonic and photonic crystal light-trapping: Architectures for optical upconversion in thin-film solar cells, *Opt. Express* **22**, A1 (2014).
- [48] E. Yablonoitch, Statistical ray optics, *J. Opt. Soc. Am.* **72**, 899 (1982).
- [49] D. Malacara and B. J. Thompson, *Handbook of Optical Engineering* (CRC Press, 2001).

- [50] A. Wang, J. Zhao, and M. A. Green, 24% efficient silicon solar cells, *Appl. Phys. Lett.* **57**, 602 (1990).
- [51] <http://www.pveducation.org/pvcdrom/design/emitter-resistance>
- [52] PV Lighthouse sheet-resistance calculator, <https://www2.pvlighthouse.com.au/calculators/Sheet%20resistance%20calculator/Sheet%20resistance%20calculator.aspx>
- [53] F. Feldmann, M. Simon, M. Bivour, C. Reichel, and M. Hermle, Efficient carrier-selective *p*- and *n*-contacts for Si solar cells, *Sol. Energy Mater. Sol. Cells* **131**, 100 (2014).
- [54] F. Feldmann, M. Bivour, C. Reichel, M. Hermle, and S. W. Glunz, Passivated rear contacts for high-efficiency *n*-type Si solar cells providing high interface passivation quality and excellent transport characteristics, *Sol. Energy Mater. Sol. Cells* **120**, 270 (2014).
- [55] G. D. Cody, T. Tiedje, B. Abeles, B. Brooks, and Y. Goldstein, Disorder and the Optical-Absorption Edge of Hydrogenated Amorphous Silicon, *Phys. Rev. Lett.* **47**, 1480 (1981).
- [56] C. Schinke, P. C. Peest et al., Uncertainty analysis for the coefficient of band-to-band absorption of crystalline silicon, *AIP Adv.* **5**, 067168 (2015).
- [57] <http://fdtd.kintechlab.com/en/fitting>
- [58] S. Bhattacharya and S. John, Designing High-efficiency Thin Silicon Solar Cells using Parabolic-pore Photonic Crystals, *Phys. Rev. Applied* **9**, 044009 (2018).
- [59] A. Cuveas, Surface recombination velocity of highly doped *n*-type silicon, *J. Appl. Phys.* **80**, 3370 (1996).
- [60] S. J. Robinson, S. R. Wenham, P. P. Altermatt, A. G. Aberle, G. Heiser, and M. A. Green, Recombination rate saturation mechanisms at oxidized surfaces of high-efficiency silicon solar cells, *J. Appl. Phys.* **78**, 4740 (1995).
- [61] A. G. Aberle, S. Glunz, and W. Warta, Impact of illumination level and oxide parameters on Shockley-Read-Hall recombination at the Si-SiO₂ interface, *J. Appl. Phys.* **71**, 4422 (1992).